

Multiscale Analysis of Plasma-Modified Silk Fibroin and Chitosan Films

Jordan Nashed^{*a,b}, Tomasz Bartkowiak^c, Alexandru Horia Marin^{d,a,f}, Tine Curk^b, and Viviana Marcela Posada-Perez^{*a,e}

^aKen and Mary Alice Lindquist Department of Nuclear Engineering, Pennsylvania State University, PA USA

^bDepartment of Materials Science and Engineering, Johns Hopkins University, MD USA

^cInstitute of Mechanical Technology, Poznań University of Technology, plac Marii Skłodowskiej-Curie 5, 60-965 Poznań, Poland

^dMaterials Science and Engineering Department, Pennsylvania State University, University Park, PA, 16802, USA

^eDepartment of Electronics and Computer Science, Pontificia Universidad Javeriana de Cali, Colombia

^fSurface Analysis Laboratory, Institute for Nuclear Research Pitesti, Mioveni, 15400, Romania

*Corresponding authors

Abstract:

Biological interactions with material surfaces span a wide range of length scales, yet conventional surface measurements often fail to account for scale, limiting the insights they provide for surface engineering. Here, we investigate how multiscale surface descriptors of plasma-modified silk fibroin and chitosan surfaces modify bacterial and immune cell response. Surface chemistry and topography were characterized using X-ray Photoelectron Spectroscopy (XPS) and Atomic Force Microscopy (AFM), followed by sliding bandpass filtration and multiscale curvature tensor-based methods to measure scale-dependent topographic features. Macrophage response and biofilm growth were assessed by fluorescence microscopy. Correlation strength showed scale-dependence with respect to surface features and biological structure: individual bacteria and small colonies correlated more strongly with fine-scale topographic features, whereas macrophage morphology correlated more strongly with larger-scale surface features. Notably, measured surface chemical descriptors generally did not correlate strongly with biofilm formation;

nonetheless, chitosan and silk fibroin showed distinct trends in bacterial support, suggesting that material identity was not captured by the measured surface properties and that prevention of biofilms likely benefits from combinatorial approaches as opposed to physical surface modification alone. These results show that different biological structures interact with material surfaces at distinct length scales, as well as demonstrate the utility of multiscale analysis in identifying scales of interest in biological interactions with surfaces. Moreover, the data suggests that tailoring topographic feature size to the characteristic scale of the targeted biological entity is a potential strategy for antibacterial wound-healing materials without incurring cytotoxicity.

Keywords: Multiscale analysis, plasma modification, biofilm, silk fibroin, chitosan, topography, surface chemistry

1. Introduction:

Chronic wounds are a major public health concern, with a global prevalence of 1.67 per 1000 population [1,2]. A key factor underlying chronic wound severity is the presence of microbial biofilms, which induce inflammation, delay healing, and incur infection [3,4]. Thus, treating chronic wounds often requires bioactive compounds to promote healing and prevent biofilm formation [5]. In particular, this has led to the adoption of silk fibroin (SF) [6–11] and chitosan (Ch) [12–14] as wound dressing materials due to their favorable healing properties and, in the case of Ch, inherent antimicrobial properties [12,14–17]. However, scientists are increasingly turning to surface modification techniques to enhance or alter the intrinsic material properties of SF [10] and Ch [18,19] to better mitigate biofilm formation while allowing host cell attachment and tissue integration. An emerging category of surface modification strategies center around physical or topographic alterations inspired by naturally-occurring bactericidal surfaces [20–22]. Although the precise mechanism of action of these bactericidal surfaces is disputed [23], it is generally recognized that high aspect ratio nanostructures are capable of killing bacteria without incurring cytotoxicity [24,25].

Our group has explored the use of a surface modification technique known as “Directed Plasma Nanosynthesis” (DPNS) as a means of creating high aspect-ratio nanostructures on biomaterial surfaces [10,19,26–28]. DPNS was first introduced by Allain et al. and later advanced for biomaterial surface modification by follow-up work from our team [10,26,29–31]. DPNS extracts ions from a plasma source and accelerates them towards a target material at low energies (~100–500 eV) and at a user-selected incidence angle, enabling the creation of oriented nanostructures on material surfaces [10,26]. Importantly, the structures created by DPNS are more complex

[10,19] than the highly-controlled patterns typically used in the study of bactericidal topographies [32–35], presenting a metrological challenge for analyzing topography quantitatively.

The biological processes relevant to wound-healing themselves are complex and occur over a large range of time and length scales. For example, protein adhesion occurs immediately after biomaterials come into contact with blood and interstitial bodily fluids, representing the very onset of the inflammatory response [36,37]. Proteins are on the nanometer scale, and their adhesion and conformation on biomaterial surfaces is largely impacted by topography at similar scales [38]. This layer of adsorbed proteins dictates subsequent cell adhesion and response [38,39]. Bacteria, on the other hand, are typically on the order of 1 μm in size [33] and are differentially impacted by nano- and micro-scale topography [19,33,35]. Individual eukaryotic cells, which are typically on the order of 10 μm in length, also respond differently to nano- and micro-scale topography, while entire cell colonies respond instead to macroscale ($> 100 \mu\text{m}$) topography [37]. The multiscale nature of both biology and surfaces themselves thus requires analysis methods which are scale-discriminant (i.e., multiscale analysis).

According to Brown et al., multiscale analysis in surface metrology can be defined as “the process of studying topographies at multiple scales of observation and comparing, merging, or associating the findings acquired from observations or calculations at different scales” [40]. This can be achieved in a number of ways, from spatial filtering to taking images at different length scales or spatial resolutions [40]. It may also involve finding the surface characterization parameters whose geometric properties are best discerned at the specific scale or scales of observations or identifying the scale or scales in which interactions between formation process and resulted surface topography or between surface topography and functional response occur [41]. Despite the apparent need for detailed multiscale analysis of surface topographies, such metrological techniques are not well-established or standardized in biomedical contexts. Studies that have explored the relationship between biological response and topographic cues at multiple scales have repeatedly demonstrated the utility of multiscale analysis in biomaterial studies [42–47]. In addition to lacking detailed multiscale information, many conventional topographic analyses fail to account for surface anisotropy [48–51]; as has been extensively and repeatedly shown, structural anisotropy greatly impacts biological response to biomaterials [10,19,37,44,44,52,53]. Finally, while qualitative descriptors of surface topographies can be useful, a more systematized, quantitative approach to characterizing surface topographies would enable more consistent comparison between studies of surfaces of arbitrary complexity [38,40].

The clinical utility of silk fibroin and chitosan, their inherent limitations, and the emergence of DPNS as a means of physical surface modification prompted our previous work investigating DPNS-treated SF [10] and Ch [19]. In the present study, we explore the capabilities of multiscale analysis in characterizing surface changes induced through plasma treatment, discriminating between treated materials, and connecting biological response to specific length scales and surface features. This goal was achieved by first collecting comprehensive data of material surface chemistry and topography via X-ray photoelectron spectroscopy (XPS) and two multiscale analysis techniques, respectively. The first multiscale method, developed by Bartkowiak et al., uses multiscale curvature tensors to estimate surface geometry at multiple scales [48]. The other, a bandpass filtration method, suppresses signal from scales outside the bandpass window and was originally applied to multiscale analysis by Berglund and Brown [54,55]. Single-scale, i.e. as-measured, topographic data was collected to compare with these multiscale methods. Surface topography and chemistry data were considered as our explanatory data. Biological data regarding the quantity and size distributions of adherent bacteria and macrophages were collected and used as response variables. Material data were analyzed to understand the material-dependent surface changes induced by DPNS as well as to compare multiscale and single-scale analysis techniques. Biological data was similarly studied to observe biological response at the material/treatment level as well as to visualize correlation with surface data as a function of scale. This study is intended to both better understand the role of topography and surface chemistry in dictating immunological and bacterial responses to SF and Ch as well as to explore the utility of multiscale analysis for the study of biomaterial surfaces.

2. Methodology

2.1 Film Synthesis

SF films were obtained following a standard LiBr-based extraction workflow [10,56]. Briefly, *Bombyx mori* cocoons were degummed in 0.02 M sodium carbonate to remove sericin, rinsed thoroughly, and dried. The resulting fibroin was dissolved in 9.3 M lithium bromide at 60°C and subsequently dialyzed (3.5 kDa Molecular weight cut-off) against ultrapure water for 48 h with multiple water exchanges. The clarified SF solution (\approx 7.8 wt/vol%) was then concentrated by osmotic dialysis against a 10% polyethylene glycol solution (PEG 10,000), yielding a viscous SF solution of \sim 15.9 wt/vol%. Films were formed by casting this concentrated solution onto glass substrates and allowing it to dry under ambient conditions.

For Ch films, a 1% (w/v) Ch solution (\geq 75% deacetylation, low molecular weight) was prepared in 1% (v/v) acetic acid using sonication and magnetic stirring. The solution was cast onto 10 \times 10

mm glass substrates (200 μ L per slide) and dried overnight at room temperature in a flow hood. The dried membranes were neutralized in 5% (w/v) sodium hydroxide for 1 h, rinsed to neutral pH, and dried again at 37 °C to obtain the final Ch films [19].

2.2 DPNS

SF and Ch films were placed in a vacuum chamber evacuated to a base pressure of 5×10^{-6} Torr and subsequently filled with argon gas to reach a working pressure of 3×10^{-4} Torr. Surface modification was performed using argon ions (Ar^+) generated from plasma at an energy of 1 keV, with a beam flux of $1.5 \times 10^{15} \text{ cm}^{-2} \cdot \text{s}^{-1}$. Following this, a second irradiation step was applied using Ar^+ ions at 500 eV with a fluence of $1 \times 10^{18} \text{ ions/cm}^2$. Treatments were conducted at incidence angles of 45° and 60°, and the resulting samples were designated as SF 45, SF 60, Ch 45, Ch 60, and their respective pristine controls (SF Control and Ch Control).

2.3 Surface characterization

For SEM analysis, cell-seeded samples were fixed, dehydrated through a graded ethanol series, stored overnight in a desiccator, and sputter-coated with iridium. Cell-free samples were cleaned, dried, and sputter-coated directly. All samples were imaged using a Thermo Scientific Verios G4 SEM or a Thermo Scientific Scios FIB under high-resolution secondary electron detection.

XPS investigations were performed using a Physical Electronics VersaProbe III instrument equipped with a monochromatic AlK_α X-ray source ($h\nu=1486.6$ eV, 200 μ m spot size) and a concentric hemispherical analyzer. The emission angle was 45. Charge neutralization was achieved with a dual-beam charge neutralization system (low-energy electrons and low-energy Ar^+ ions). Before the experiments, the binding energy scale of the spectrometer was calibrated by setting the Fermi edge of sputtered gold to 0 eV and the $\text{Au}4\text{f}_{7/2}$ line to 84.0 eV. The acquired high-resolution spectra were charge referenced by fixing the C1s peak of aliphatic carbon at 285.0 eV [57]. Measurements were made at a takeoff angle of 45 with respect to the sample surface plane.

Five AFM images per treatment condition were obtained for both SF and Ch films, resulting in thirty total images. Images were obtained using Bruker's Icon Dimension II or Bruker's Icon AFM-IR, both in PeakForce tapping mode. Images were all acquired at 5×5 μ m and 512×512-pixel resolutions to enable consistent comparison and multiscale analysis between all images.

2.4 Bacterial Growth

Escherichia coli (E. Coli) was cultured in tryptic soy broth at 37°C under mild agitation (50 rpm) for 24 h. The culture was subsequently diluted to a final concentration of $\sim 26 \times 10^6$ CFU/mL. Each

sample was exposed to 2 mL of the bacterial suspension and incubated at 37 °C for 1 h under static conditions. Following incubation, nonadherent bacteria were removed by rinsing samples with phosphate-buffered saline. The remaining surface-bound bacteria were stained using SYTO 9. Fluorescence imaging was performed using a confocal microscope equipped with FITC (excitation/emission: 480/500 nm) filter. In another set of samples bacteria were fixed and dehydrated with consecutive ethanol dilutions in water. The samples with the bacteria cells were coated with iridium and SEM images were obtained using a Verios G4.

Bacterial proliferation was quantified in ImageJ via statistics gathered from ImageJ's "particle analyzer". These statistics are the fractional area of the image covered by bacteria (denoted as area coverage) and the area density of small, medium, and large bacterial colonies, which were defined as falling between 1-20 μm^2 , 20-200 μm^2 , and > 200 μm^2 , respectively. This approach was taken due to the extreme skewness of the colony size distribution (**Figure S2**) as well as the biological motivation to observe the differential effect of DPNS on individual bacteria (i.e., small colonies) and large biofilms. All bacterial statistics were normalized by the area of the analyzed region.

These data were obtained by first selecting a square region of interest (ROI) from a fluorescence image, subtracting the background using 50.0 pixel rolling ball radius with sliding paraboloid and no smoothing before applying a threshold, whose value was determined visually such that none of the observed bacteria were removed. After thresholding, ImageJ's particle analyzer created a ROI which could be pasted onto the original grayscale 8-bit image for subsequent measurement. A list of particle sizes was then obtained along with the total area covered by the identified particles.

2.5 Macrophage morphology

Macrophages were fixed with 4% paraformaldehyde, permeabilized with 0.1% Triton X-100, and blocked with 2% BSA. Cells were incubated with rabbit anti-CCR7/CD197 (Bioss, bs-1305R) and rat anti-CD206 (MR5D3; Invitrogen, MA5-16871) following a standard secondary-detection protocol (overnight at 4 °C), with buffer-only controls included. After three PBS washes, samples were incubated with FITC-conjugated goat anti-rabbit IgG (Invitrogen, A16118) for CCR7 and Alexa Fluor™ 633 goat anti-mouse IgG2a (Invitrogen, A-21136) for CD206. Nuclei were counterstained with DAPI, and samples were imaged under fluorescence microscopy. Merged fluorescence masks were used to quantify macrophage coverage and clustering. Clusters were defined as spatially contiguous macrophage-positive regions (connected components) within the

merged mask. ImageJ's particle analyzer was used to derive area distribution statistics from macrophage clusters.

2.6 Multiscale Topographic Analysis

2.6.1 Image Processing

Raw AFM images were initially processed in Gwyddion 2.63. First, mean plane subtraction was applied. If scan line artifacts or scars were present, Gwyddion's "align rows" tool was implemented using polynomial of degree one followed by the "correct horizontal strokes" tool. All images were adjusted to set the minimum height value to 0 nm before further processing. A MATLAB script was written to convert files from Gwyddion into the format needed for multiscale curvature analysis in Mathematica. The MATLAB and Mathematica scripts are available upon request and pseudocode for the Mathematica script is available in [58].

2.6.2 Multiscale Curvature Tensor Method

Text files of the processed images were analyzed using the Mathematica script produced by Bartkowiak et al. [48], wherein each AFM image was analyzed at eight different scales increasing linearly from \sim 10 nm to \sim 0.5 μ m. These scales are distinct from those in the bandpass filtration method due to the fundamental difference in how scale is defined in each method. A schematic depiction of the curvature computation is shown in **Figure 1a**. From the multiscale tensor method, 15 parameters related to surface curvature were computed and analyzed. These fifteen parameters were grouped into two families, complexity and signed curvature. Complexity refers to changes to topographic parameters with scale as well as irregularity/changes in curvature. Signed curvature is the average 'character' of a surface's curvature; positive signed curvature indicates higher peak character while negative signed curvature indicates increased valley character. Individual variables, their definitions, and assigned families are described in the (**Supporting Information, Appendix A**).

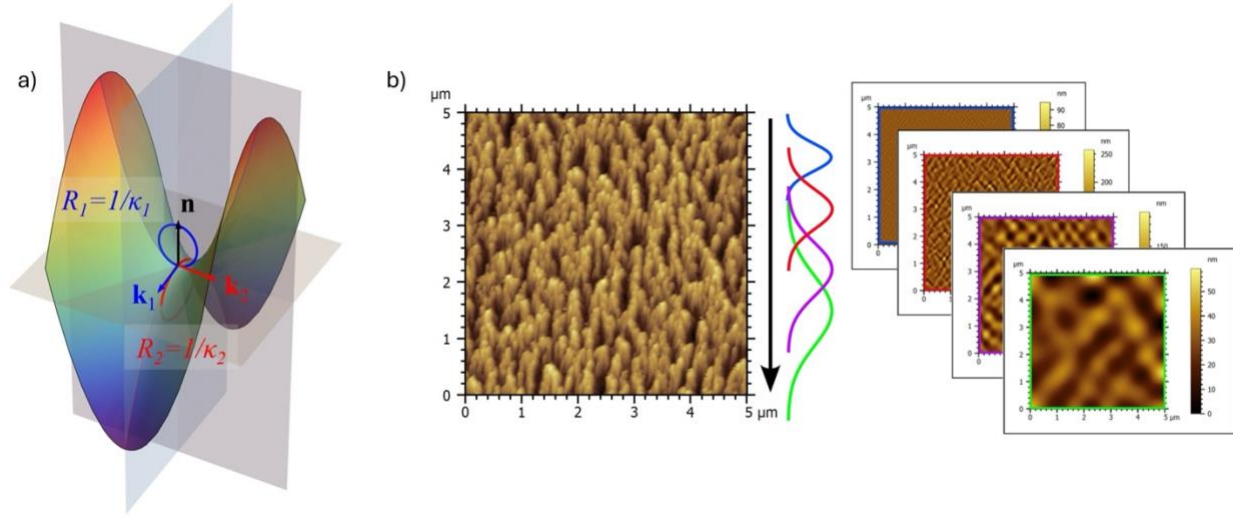


Figure 1. Multiscale methods description. a) Schematic representation of the principal curvatures κ_1 and κ_2 , calculated at an example saddle-like location, used in the multiscale tensor method. b) Example of the sliding bandpass filtration approach, showing the raw AFM topography and a series of filtered images at different scales.

2.6.3 Sliding Bandpass Filtration Method

Sliding bandpass filtration was applied in MountainsMap 11 (Digital Surf, France) Free Trial software using the ‘bandpass filter bank’ operator with first-order ISO Gaussian filters, two bands per octave, and automatic cutoffs. This effectively resulted in fourteen images – one unfiltered, and thirteen filtered – for each of the thirty raw AFM images acquired. Sliding bandpass filtration is shown in **Figure 1b**. From each of these images, 29 ISO standard parameters were collected to holistically characterize the surface topography (**Supporting Information, Appendix A**). For ease of analysis and interpretation, these parameters were grouped into ten different families: Anisotropy, Void Volume, Hill Volume, Void Area, Hill Area, Projected Area, Roughness, Complexity, Peak Curvature, and Void Curvature. Scale here is interpreted as the central wavelength of the bandpass filter.

2.6.4 Single-scale Analysis

Single-scale analysis was performed by calculating the same ISO parameters and families used in the bandpass method on unfiltered AFM images.

2.6.5 Analyzing Topographic Changes

AFM images were examined to gain insight into the morphological changes induced by plasma treatment (**Figure 2a-f**). These qualitative observations were supplemented by plotting several multiscale topographic parameters as a function of scale (**Figure 2g-l**).

2.6.6 Visualizing Group-Level Surface Changes: PCA

Principal Component Analysis (PCA) was performed on the single-scale topography plus XPS data as well as on the multiscale topography plus XPS data to visualize group-level differences in material surface properties. Each of the thirty total samples' scores were plotted on PC1 and PC2 to visualize their grouping in latent space. Since PC1 captured most of the variance in material data and was most discriminatory with respect to material and treatment for both single-scale and multiscale data, its loadings were investigated explicitly to better understand the latent structure in the surface data. To accomplish this, the top two largest loadings per family were plotted and visualized.

2.6.7 Visualizing Correlation with Biological Data: Heat Maps

Heat maps were created to visualize correlation of material parameters with biological response as a function of surface chemistry, topographic feature, and, in the case of multiscale data, scale of observation. Chemical data was first normalized to ensure fair comparison between material and treatment conditions. This involved taking the chemical state relative concentrations (**Tables 1 and 3**) and multiplying them by their respective element relative concentrations (**Table 2**) for each material and sample to normalize for atomic concentration. The analyzed functional groups from the C1s peak were C-C/C-H, C-N/C-O/C-NH₂, C-N-C=O/C=O, R-O-C=O/C-N₃, and pi to pi* shakeup; from the N1s peak, NH₃⁺ was analyzed. For topographic data, parameters were sorted into several families (**Supplementary Information, Appendix A**), where a particular family represented a shared characteristic captured by its constituent parameters. This family-level grouping was employed for several reasons: 1) variables within families often had very strong collinearity, making separation of variables within a family redundant and uninformative, 2) interpretation was vastly improved by this dimensionality reduction, and 3) grouping variables from a given family helped mitigate spurious correlation. Bandpass and multiscale curvature tensor data were separated due to the differences in their respective scale measurements.

Data for each feature was mean-centered and reduced to unit variance (i.e., Z-scored) to normalize units. Each sample's data was then averaged within each family (and scale bin, in the case of multiscale data) to give a sample-level score per family. Sample scores were group-wise

averaged to give a group-level (i.e., SF 45, SF Control, etc.) score for a particular family and scale. Biological data was group-wise averaged for determination of Spearman's rho in subsequent steps. Spearman's rho was selected as the correlation metric because it strictly is concerned with monotonicity in the relationship between material and biological data (as opposed to the linearity, as in Pearson's r). This quality made Spearman's rho ideal since the relationships between material and biological data may, in general, be nonlinear. If a given family contained no variables after the statistical significance screening, its cells were greyed out in the final heatmap. To mitigate spurious correlation in the multiscale data, if correlation values for a given family differed by more than 1.0 at adjacent scales of observation, those cells were similarly greyed out.

3. Results and Discussion

3.1 Impact of DPNS on Material Surface Properties: Observations from Raw Data

3.1.1 Topographic Changes

Most nanoscale studies, especially those correlating biological variables, rely on a single scale for the interpretation of topography [59,60]. However, multiscale events occur simultaneously on the surface when they are in contact with biological entities; therefore, nano-, micro-, and mesoscale features often need to be considered for more detailed insight. We induced topographic changes on the material surfaces via Ar^+ irradiation, which mainly introduced topographical changes along with soft or mild chemical modifications.

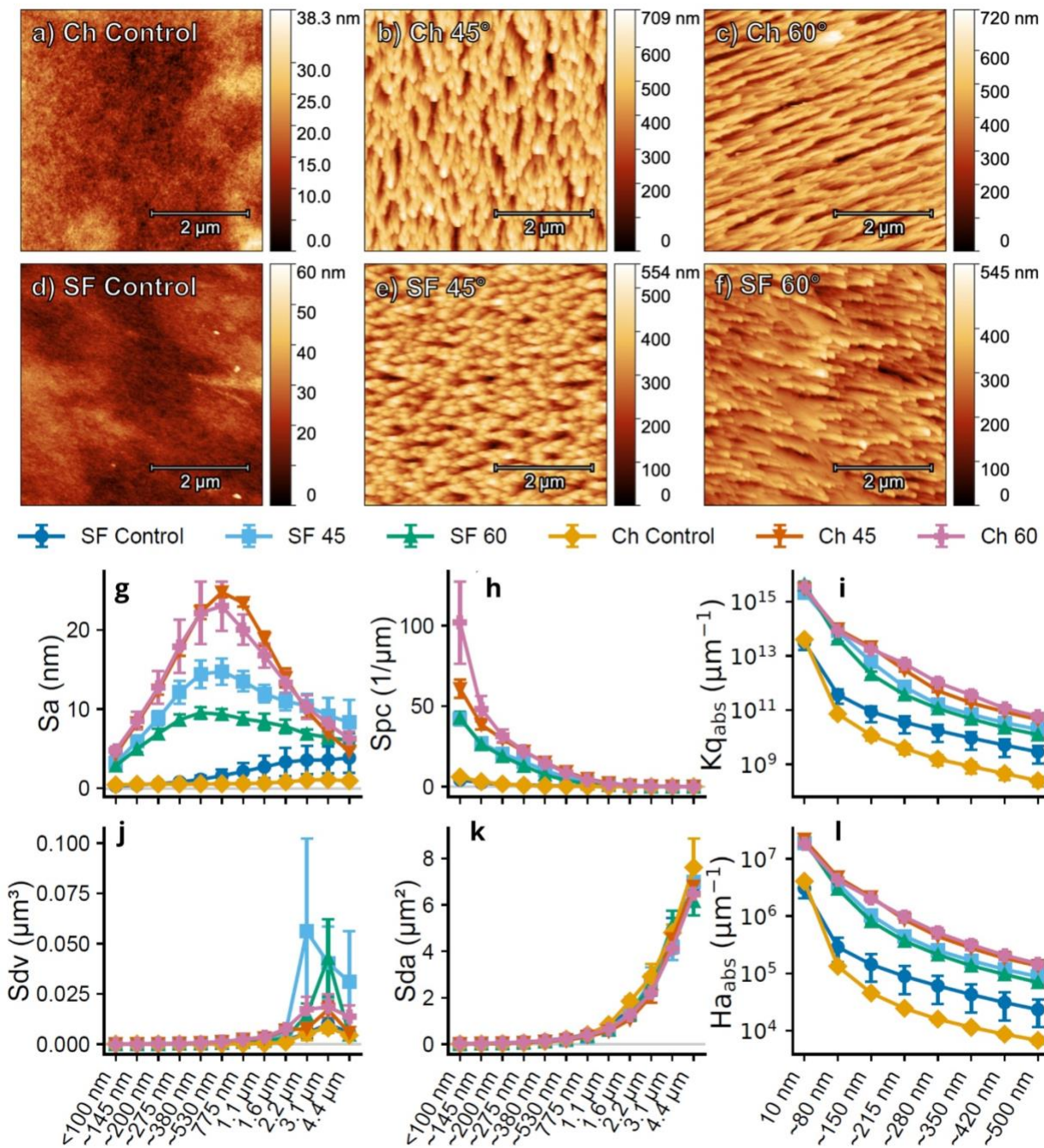


Figure 2. Angle-induced topography changes in Ch and SF surfaces. 5x5 μm AFM images for chitosan (Ch) and silk fibroin (SF) under control conditions and after treatments at 45° and 60° (a-f). The images show how the incidence angle drives changes in surface morphology and nano-feature organization. Panels (g-l) present the quantified surface-texture parameters: g) mean

roughness (Sa), h) mean peak curvature (Spc), i) standard deviation in absolute Gaussian curvature (Kq_{abs}), j) mean void volume (Sdv), k) mean void area (Sda), and l) average absolute curvature (Ha_{abs}) as a function of scale (note: bandpass scale axis is nonlinear due to binning algorithms). The curves compare the effect of treatment angles across material surfaces.

Irradiation created major topographic alterations in both materials, as shown in the AFM scans in **Figure 2 (a–f)**. Off-incidence ion irradiation produced an oriented “grass-like” morphology, as previously observed in our reports and in the literature [10,19,61]. The anisotropy of these structures increased with irradiation angle, again consistent with previous results [10,19]. Multiscale analysis showed that increasing the irradiation angle reorganized surface complexity rather than uniformly amplifying roughness, shifting curvature density toward smaller scales.

Key multiscale parameters extracted from the AFM scans were plotted as a function of scale in **Figure 2 (g–l)**. Notably, the average roughness (Sa) peaks at intermediate scales, from 200 nm – 1.6 μ m, giving an estimate for the scale at which the tallest structures (i.e., the oriented nanostructures) were formed. Treated Ch showed higher roughness than treated SF, irrespective of irradiation angle. Mean peak curvature (Spc) increased with decreasing scale for all treated materials, indicating a high degree of nano-scale asperities introduced by irradiation. Treated Ch exhibited the highest mean peak curvature. Mean dale volume (Sdv) was expectedly largest at the largest scales and was highest for treated SF. Mean void area (Sda) was highly consistent among all six groups and decreased with scale.

From the multiscale curvature tensor data, similar but distinct trends were observed. Root mean square (RMS) absolute Gaussian curvature (Kq_{abs}) and absolute mean curvature (Ha_{abs}) both increased significantly with decreasing scale, indicating a high degree of topographic complexity and curvature at small scales, particularly for treated materials.

Single-scale data (**Supplementary Figure S1**) corroborated the above findings, though lacking the added depth provided by multiscale analysis. Single-scale measurements suggested that Ch was rougher, but multiscale analysis revealed that this roughness occurred primarily from ~300–1 μ m, near the characteristic scale of individual bacteria [34]. In this regard, treated Ch exhibited the highest average roughness, peak curvature, and void volume. Control SF, on the other hand, had the largest mean void area, which differed significantly from the multiscale data. This discrepancy is likely due to the identification of fewer, larger dales in SF Control compared to Ch Control, as determined by the watershed algorithm used to compute Sda in the single-scale data. Interestingly, bandpass filtration largely mitigated this discrepancy. Overall, the topographic data

showed that DPNS induced a higher degree of nanostructuring in Ch compared to SF, with the characteristic scale of the oriented nanostructures ranging from 200 nm to 1.6 μ m. This scale range overlaps with the dimensions relevant to bacterial bodies and appendages [62,63]. Moreover, topographic complexity and curvature at the smallest scales increased significantly with treatment.

3.1.1.1 Discriminating Surfaces: Principal Component Analysis

To demonstrate that multiscale surface descriptors capture treatment-specific signatures that are not resolved by single-scale metrics, principal component analysis (PCA) was employed to assess the ability of the measured surface properties to differentiate between the six material–treatment groups. PCA of the material data helped elucidate the discriminating surface features defining the treatment/material groups for both single-scale and multiscale datasets (**Figure 3**). Closeness in this space indicates a high degree of similarity in the measured surface parameters.

PCA was expectedly better able to distinguish between groups using multiscale data than single-scale data, as indicated by the increased separation between the six groups in the plots, particularly for the 45-degree irradiated samples. PC1 captured much of the variance in surface data and was the most discriminatory for both single- and multiscale datasets. Therefore, PC1 loadings were investigated to understand the essential latent structure encoded by PC1 and thus the latent structure differentiating the material surfaces (**Figure 4**).

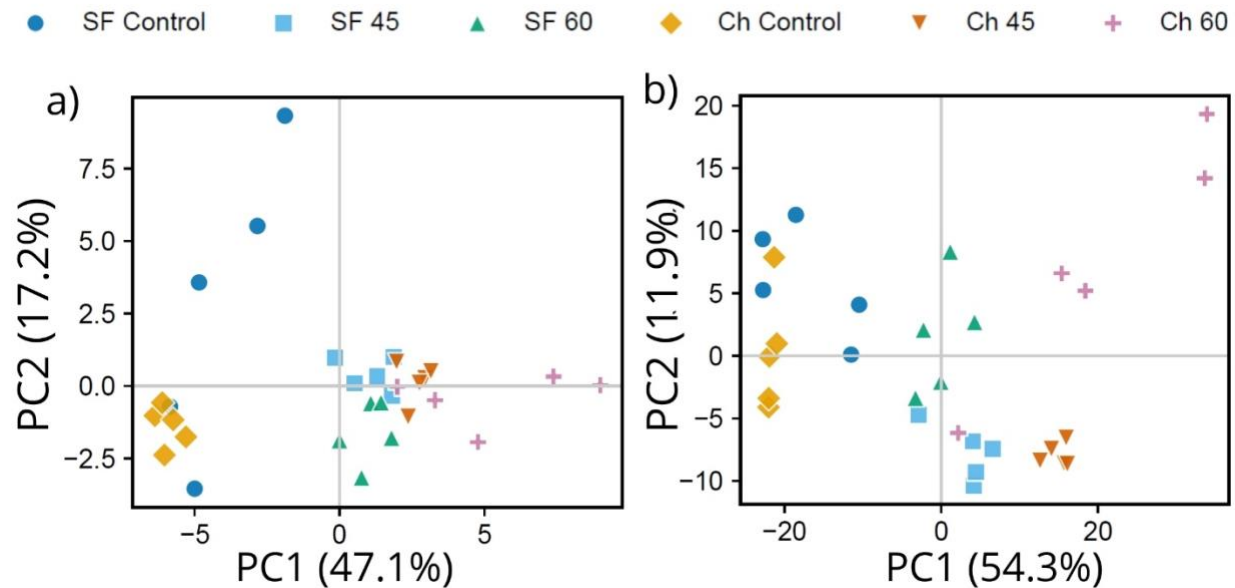


Figure 3. PCA score plots for (A) single-scale and (B) multiscale surface-parameter datasets with captured variance (%) for each principal component listed. The distributions highlight how control, 45°, and 60° treatments cluster for both silk fibroin (SF) and chitosan (Ch) samples, showing the separation driven by angle-dependent topographic features. Principal component 1 (PC1) captured nearly half the variance in both datasets. A higher value of PC1 indicates increased nanostructuring and is a proxy for DPNS treatment.

PC1 loadings are shown in **Figure 4**. Single-scale data had positive loadings for parameters associated with nanostructuring (i.e., roughness, volume, area, and complexity), ester/azide concentration, and (correcting for sign conventions) anisotropy and void curvature. Notable negative loadings were associated with amide/carbonyl concentration. Therefore, positive PC1 scores were indicative of higher degrees of nanostructuring and a relative increase in ester/azide concentration compared to amide/carbonyl concentration. Amide/carbonyl concentration decreased with treatment, while ester/azide concentration as well as nanostructuring increased with treatment (**Supplementary Figure S3**). Therefore, PC1 was effectively a proxy for DPNS treatment. Multiscale loadings exhibited similar trends; factors associated with nanostructuring dominated the positive loadings and ester/azide concentration was opposite the loading for amide/carbonyl concentration. Loadings were largely uniformly distributed along scales for each given parameter, likely due to strong multicollinearity and the large number of variables.

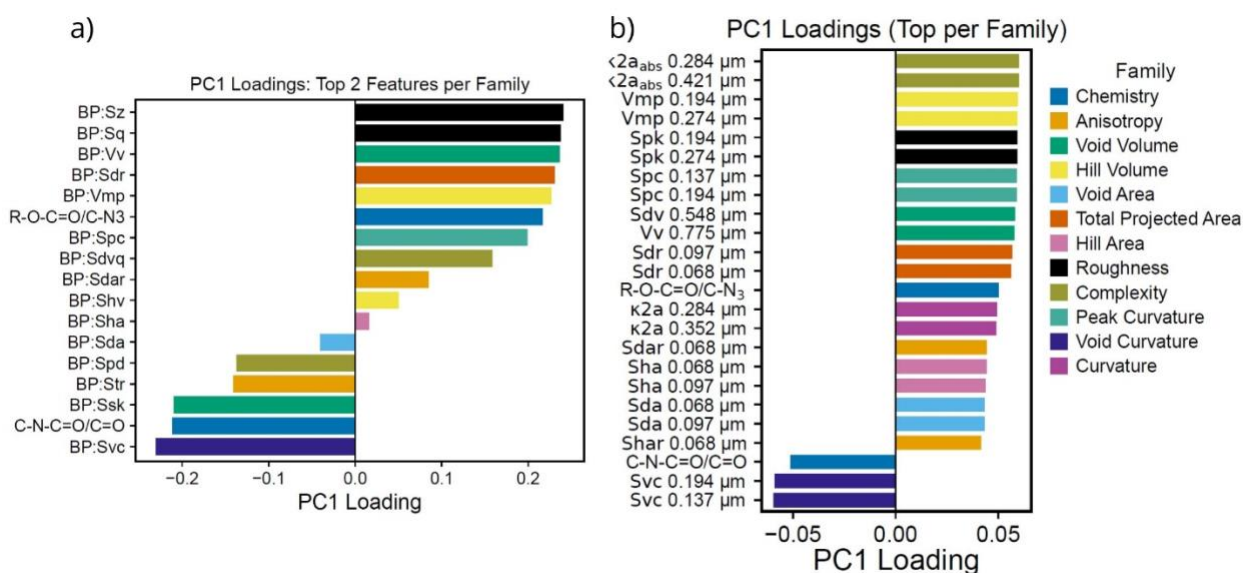


Figure 4. PC1 loadings for the top two features within each functional family. The left panel (A) shows the highest-loading parameters from the multiscale dataset (502 total parameters), while the right panel (B) shows the corresponding top features from the conventional (single-scale) dataset (35 total parameters). Colors denote the functional family associated with each parameter.

Importantly, PC1 emerged as a latent multiscale surface signature rather than a simple roughness index, integrating curvature, void structure, anisotropy, and complexity across scales. The relatively uniform distribution of loadings reflects strong multicollinearity among scale-resolved descriptors and suggests hierarchical surface restructuring rather than dominance of a single scale. In this sense, multiscale analysis does not introduce redundant information but reveals coordinated reorganization of surface features across length scales. Although chemical parameters contributed less to the total variance, their alignment with PC1 indicates that near-surface chemical changes follow the same multiscale trend, as further examined by XPS in the following section.

3.1.2 Surface Chemistry

The surface chemistry of Ch was explored using XPS by comparing an untreated control with plasma-irradiated samples exposed to a fluence of 1×10^{18} ions/cm² at irradiation angles of 45° and 60° to identify the surface functional groups induced or modified by plasma treatment. In line with the multiscale PCA results, these XPS measurements indicate that plasma irradiation induces systematic but comparatively subtle chemical changes that evolve consistently with the treatment-dependent surface restructuring.

Figure 5a illustrates the nitrogen chemical behavior as a function of argon plasma irradiation angle, with the observed broadening of the overall N1s spectrum indicating variations in chemical states relative to the untreated Ch. After extracting the binding energy positions through the curve-fitting of the N1s signal, its corresponding chemical states were identified (**Figure 5b-d**, Table 1). Therefore, the spectral features located at 399.4 ± 0.2 eV [30,57,64,65] and 400.3 ± 0.2 eV [30,57,66], appearing only for the control Ch, are attributed to C-NH₂ and C-N-C=O groups. At this stage, it is noteworthy that the 75.5% fraction of non-protonated amine observed in the control sample (Fig. 1b, Table 1) closely matches the nominal degree of acetylation specified for the commercial Ch [67]. Moreover, the quantitative analysis yields an atomic ratio of O to N of 4.5, and of C to O of 2.3, both slightly higher than the expected stoichiometric values of 4.0 and 1.5, respectively, for Ch, $[(C_6H_{11}NO_4)_n]$ [68].

The elevated C/O ratio presumably came from adventitious surface contamination. Next, the nitrogen chemical response of Ch to the plasma treatment conditions was linked to the creation of two additional functional groups, namely N=C and NH₃⁺ for the 45-degree irradiation and NH₃⁺ and NH₄⁺ for the 60-degree irradiation, with their corresponding binding energies located at 398.0±0.2 eV [69–72], 401.1±0.2 eV [30,64,65,67,73], and 402.6±0.2 eV [74–77], respectively. More specifically, plasma irradiation induced surface amination and protonation, resulting in the incorporation of NH₄⁺ functionalities exclusively at higher irradiation angles (**Figure 5c-d, Table 1**). In terms of atomic fractions, the free amine content decreased by approximately half in both cases, dropping from ~75% to 34% and 39%, respectively (**Figure 5b-d**, Table 1). At the same time, the O/N ratio decreased, from 4.5 to 2.4 (**Table 2**).

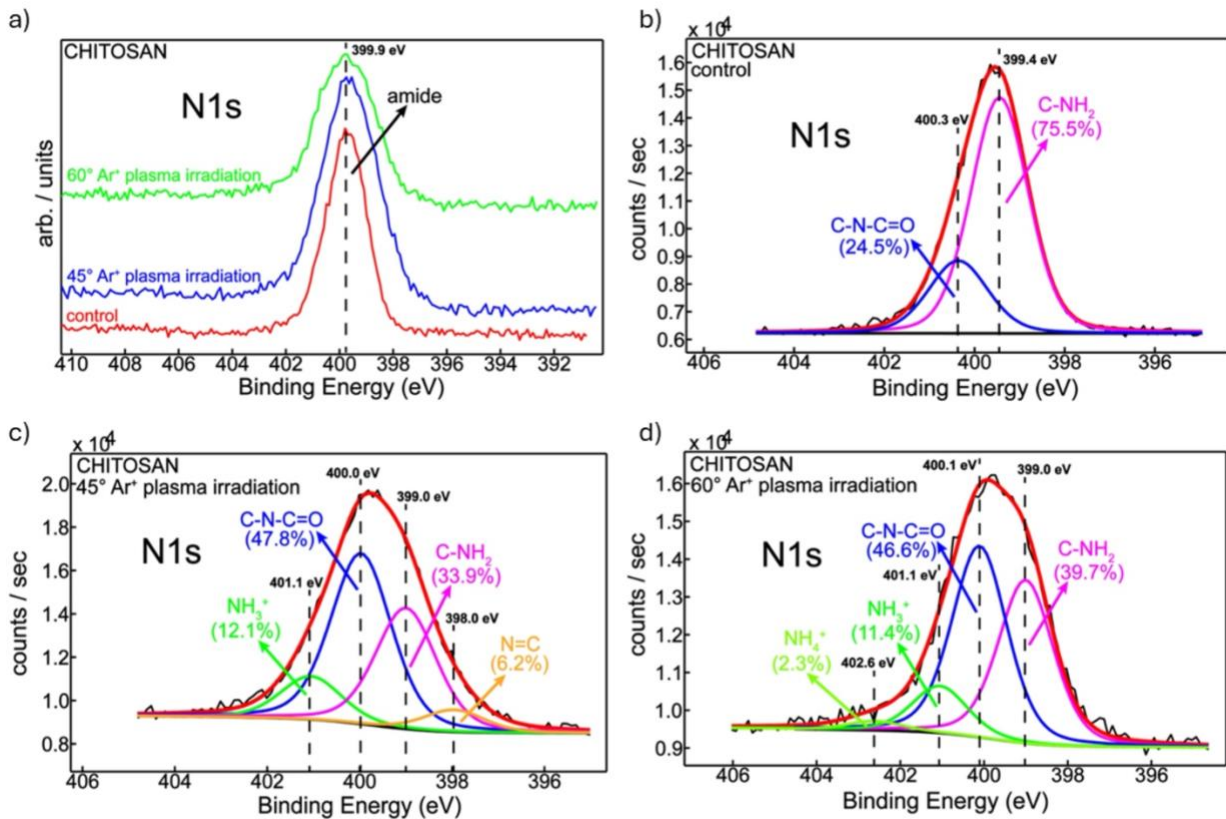


Figure 5. N1s XPS superimposed spectra of the Ch before and after Ar⁺ plasma irradiation (a); N1s XPS peak-fitted spectrum of the Ch before Ar⁺ plasma irradiation (b); N1s XPS peak-fitted spectrum of the Ch after 45° Ar⁺ plasma irradiation (c); N1s XPS peak-fitted spectrum of the Ch after 60° Ar⁺ plasma irradiation (d).

Table 1. Nitrogen chemical table: chemical species, binding energies, and chemical state relative concentrations.

Ch	Nitrogen chemical species	Binding energy	Nitrogen chemical states relative conc.
		[eV]	[%]
control	C-NH ₂	399.4	75.5
	C-N-C=O	400.4	24.5
45° Ar ⁺ irradiation	N=C	398.0	6.2
	C-NH ₂	399.0	33.9
	C-N-C=O	400.0	47.8
	NH ₃ ⁺	401.1	12.1
60° Ar ⁺ irradiation	C-NH ₂	399.0	39.7
	C-N-C=O	400.1	46.6
	NH ₃ ⁺	401.1	11.4
	NH ₄ ⁺	402.6	2.3

Further, **Figure 6a** presents the carbon spectra of Ch before and after plasma treatment, highlighting the general trend with an increasing irradiation angle. At first glance, the amine and amide groups show a visible decrease, accompanied by a pronounced increase in aliphatic carbon species. In addition, the former observation is consistent with the decreasing trend of nitrogen amines (**Figure 5, Table 1**).

For a more refined perspective, the C1s peak signal was decomposed into its components with binding energies of 284.9±0.2 eV [57,78,79], 286.4±0.2 eV [57,78,79], 288.0±0.2 eV [57,78,79], 289.5±0.2 eV [30,79], and 291.0±0.2 eV [30,80], characteristic of C-C/C-H, C-O/C-NH₂, C=O/C-N-C=O, O-C=O/C-N₃ bonds and shake-up satellite, respectively. Quantitatively, the fraction of non-protonated amines decreases with an increasing irradiation angle, nearly halving from 45.4% to 23.3% (**Figure 6b-d, Table 3**). This trend aligns well with the above nitrogen chemical behavior, which implies a similar reduction in the amine content (**Figure 5, Table 1**). On the other hand, the C-to-O ratio increases with the angle of irradiation (**Table 2**), accompanied by a decrease in the C-O chemical bond, which cannot be completely ruled out (**Figure 6b-d, Table 3**).

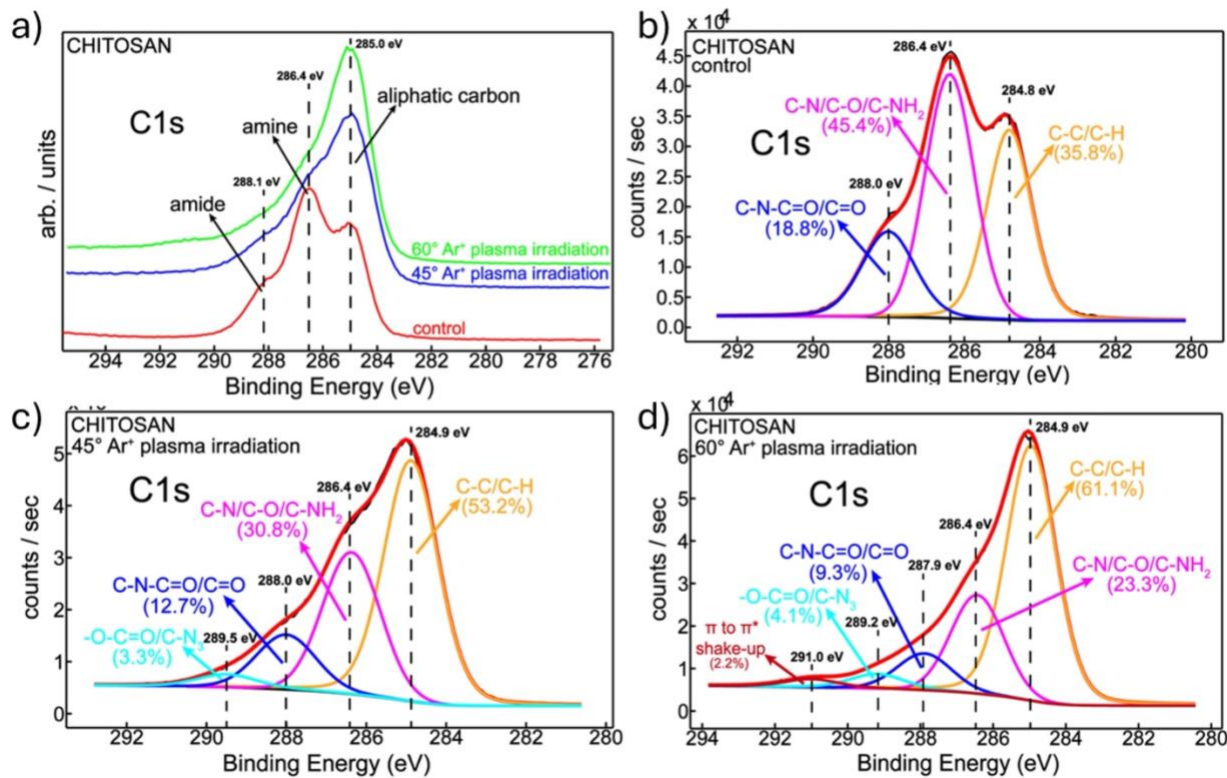


Figure 6. C1s XPS superimposed spectra of the Ch before and after Ar⁺ plasma irradiation

(a); C1s XPS peak-fitted spectrum of the Ch before Ar⁺ plasma irradiation (b); C1s XPS peak-fitted spectrum of the Ch after 45° Ar⁺ plasma irradiation (c); C1s XPS peak-fitted spectrum of the Ch after 60° Ar⁺ plasma irradiation (d).

Table 2. Element relative concentrations (at. %).

Ch	C1s	N1s	O1s	C/O atomic ratio	O/N atomic ratio
control	65.2±6.5	6.3±0.6	28.5±2.8	2.3	4.5
45° Ar ⁺ irradiation	68.8±6.8	8.7±0.8	22.5±2.2	3.1	2.6
60° Ar ⁺ irradiation	78.6±7.8	6.3±0.6	15.1±1.5	5.2	2.4

In terms of atomic balance, specifically the comparison between the total number of atoms and the fraction that are chemically bonded, we obtained the following results, derived from oxygen quantification using both elemental and carbon curve-fits, where the summed areas of the nitrided and oxidized carbon peaks, normalized to the total carbon signal should equal the ratio of oxygen and nitrogen concentrations to carbon [30,81], and only minor differences were observed:

Control: $(6.3+28.5)/65.2=0.53$; $(45.4+18.8)/100=0.64$

45° Ar⁺ irradiation: $(8.7+22.5)/68.8=0.45$; $(30.8+12.7+2*3.3)/100=0.50$

60° Ar⁺ irradiation: $(6.3+15.1)/78.6=0.27$; $(23.3+9.3+2*4.1)/100=0.40$

Table 3. Carbon chemical table: chemical species, binding energies, and chemical state relative concentrations.

Ch	Carbon chemical species	Binding energy [eV]	Carbon chemical states relative concentrations [%]
control	C-C/C-H	284.8	35.8
	C-N/C-NH ₂	286.4	45.4
	C-N-C=O/C=O	288.0	18.8
45° Ar ⁺ irradiation	C-C/C-H	284.9	53.2
	C-N/C-NH ₂	286.4	30.8
	C-N-C=O/C=O	288.0	12.7
	-O-C=O/C-N ₃	289.5	3.3
60° Ar ⁺ irradiation	C-C/C-H	284.9	61.1
	C-N/C-NH ₂	286.4	23.3
	C-N-C=O/C=O	287.9	9.3
	-O-C=O/C-N ₃	289.2	4.1
	$\pi-\pi^*$ shake-up	291.0	2.2

Since this is a follow-up study of our previous work [30], where we comprehensively examined the plasma-induced chemical changes in SF under identical experimental conditions, **Figure 7** presents only a direct comparison between Ch and SF as a function of irradiation angle.

Therefore, a close inspection of the carbon signals reveals a completely different chemical profile for the control samples (**Figure 7a** and **b**). Specifically, Ch exhibits a clear enrichment in amine groups, while, at the same time, SF shows an increase in amide functionalities (**Figure 7a**), which is in turn consistent with the corresponding enhancement of nitrogen-bound amides in the latter (**Figure 7b**). Furthermore, the enrichment of amide groups in SF remains evident after 45° and 60° plasma irradiation, accompanied by a corresponding increase in amine groups in Ch (**Figure 7c,e**). From the nitrogen perspective, the amide contribution in SF increases after plasma treatment and becomes more pronounced at higher irradiation angles (**Figure 7d,f**). Simultaneously, its amine contribution reaches a higher level at 45° (**Figure 7d**), in agreement with the corresponding carbon chemistry (**Figure 7c**).

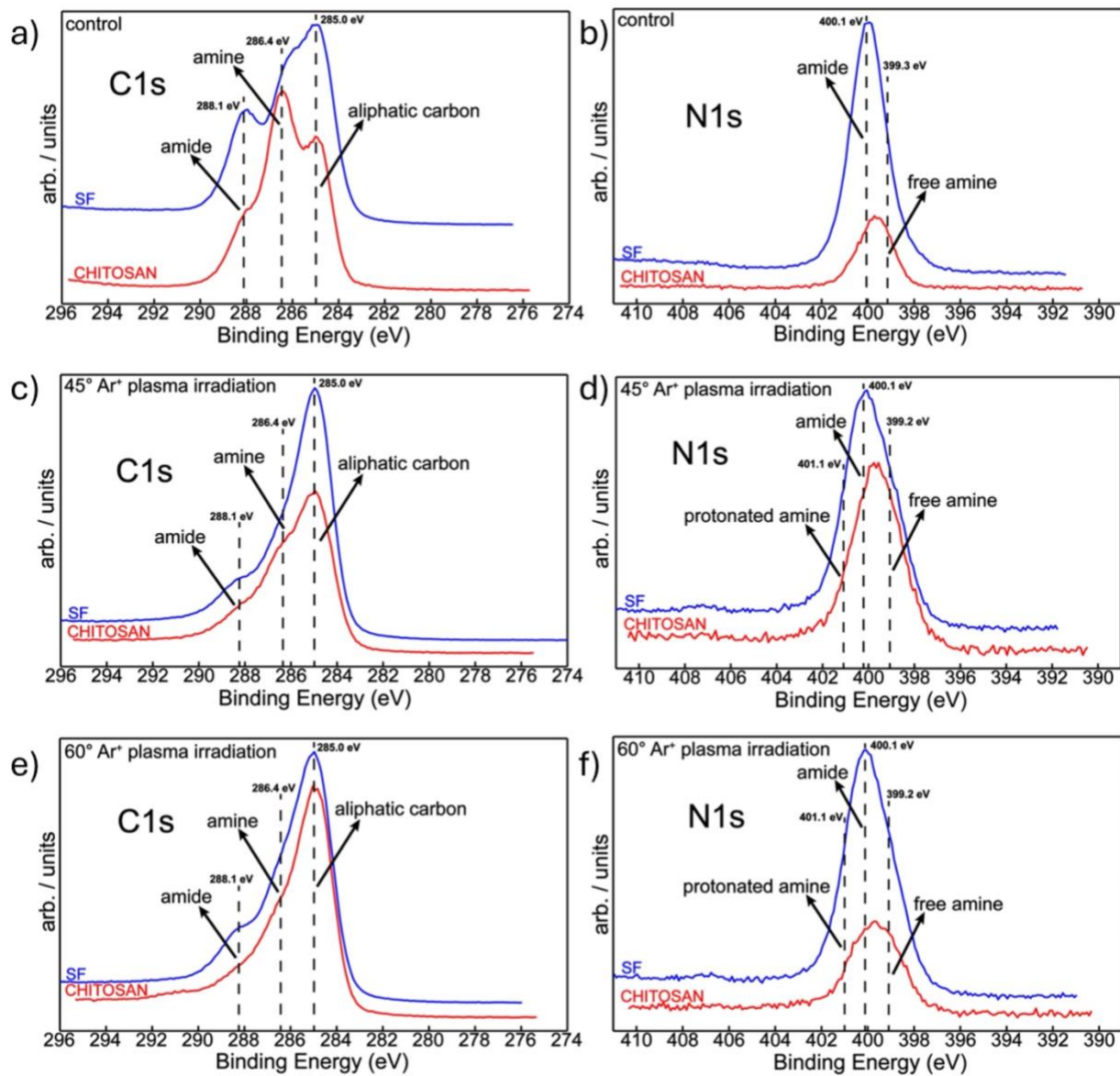


Figure 7. C1s XPS superimposed spectra for the Ch and SF: (a) control; (c) after 45° Ar^+ plasma irradiation; (e) after 60° Ar^+ plasma irradiation; N1s XPS superimposed spectra for the Ch and SF: (b) control; (d) after 45° Ar^+ plasma irradiation; (f) after 60° Ar^+ plasma irradiation.

3.2 Biological Response to DPNS-Treated Surfaces

3.2.1 Surface-Dependent Bacterial Attachment Behaviors from Nano- to Mesoscale

To compare attachment behaviors between the two materials and further describe the emerging multiscale correlation, we evaluated representative surface conditions for both SF and Ch. SF

Control samples exhibited a well-developed and cohesive biofilm (**Figure 8a**). SF 45 showed larger and more closely spaced clusters (**Figure 8b**), whereas SF 60 displayed predominantly isolated bacteria with reduced aggregation (**Figure 8c**). In this context, SEM and fluorescence imaging (**Figure 8e-h**) probe different but complementary length scales. SEM captures nanoscale and microscale attachment features that are locally informative but spatially limited, whereas fluorescence imaging integrates these events over larger areas, enabling mesoscale quantification of area coverage and colony size. The combined use of both techniques therefore supports a multiscale interpretation of attachment behavior, rather than a one-to-one comparison between imaging modalities.

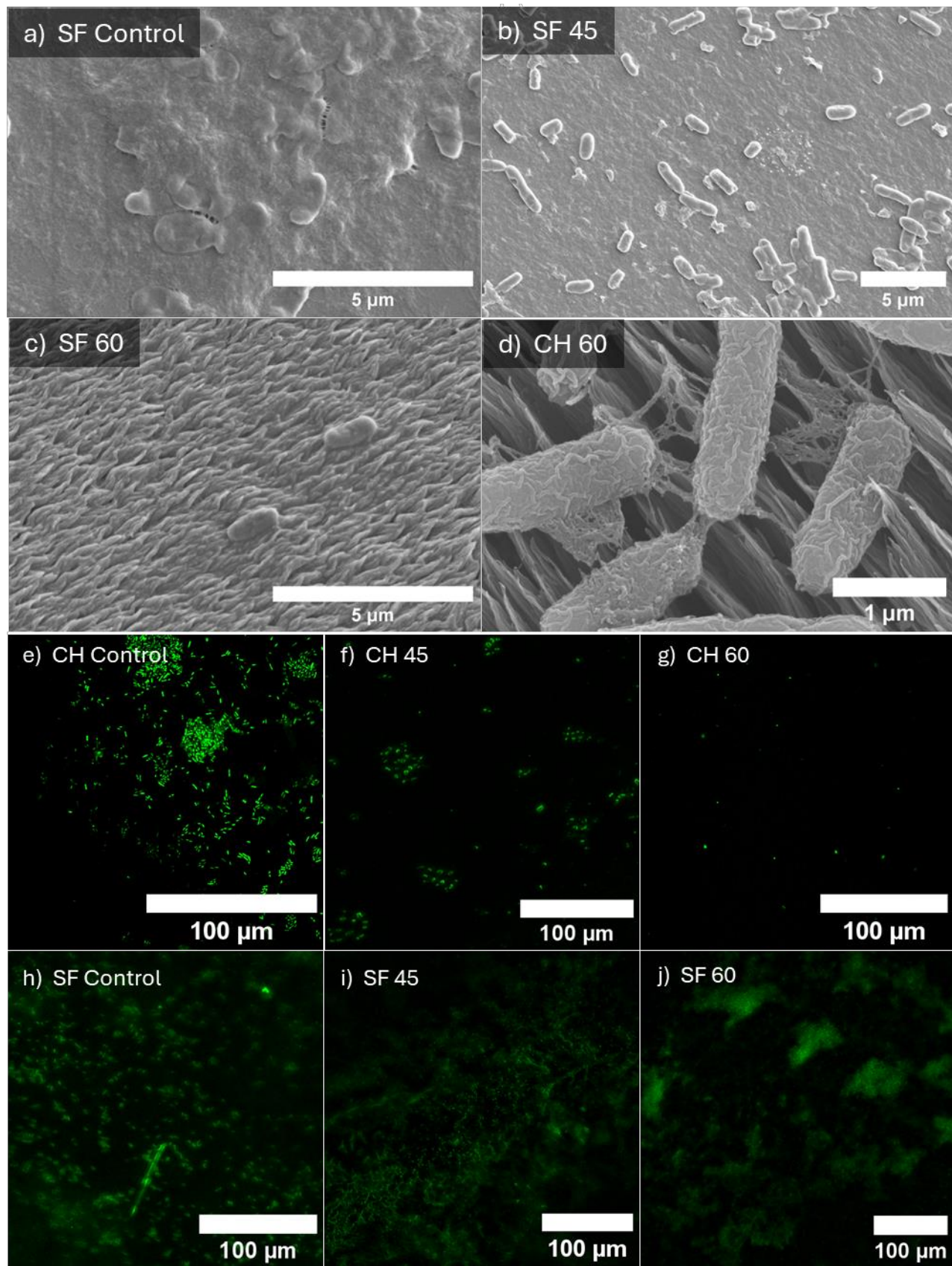


Figure 8. Multiscale bacterial attachment on silk fibroin (SF) and chitosan (Ch) surfaces. Representative SEM images showing bacterial adhesion on (a) SF Control, (b) SF 45, (c) SF 60, and (d) Ch 60. Panel (d) corresponds to a higher-magnification view highlighting local cell–surface interactions on Ch 60. Fluorescence images stained with SYTO 9 illustrate bacterial attachment patterns on (e) Ch Control, (f) Ch 45, (g) Ch 60, (h) SF Control, (i) SF 45, and (j) SF 60, capturing mesoscale organization over larger surface areas. Scale bars are indicated in each panel. Panels (d), (e), and (g) are adapted from [19] with permission. Copyright © 2023 American Chemical Society.

In contrast, Ch surfaces (previously characterized in [19]) revealed distinct attachment modes across their respective nanoscale features. Ch Control presented flat clusters without evidence of a mature biofilm. Samples with small nanostructures exhibited dispersed clusters with early polysaccharide-like material and occasional pili, while Ch-60 showed bacteria positioned between nanostructures, extending appendages across nanoscale features and displaying more prominent flagella (**Figure 8d**).

Together, these qualitative patterns align with the multiscale attachment mechanisms described for *E. coli*. While a detailed mechanistic description of bacterial attachment is beyond the scope of this work, the following observations are discussed in terms of potential correlations between multiscale surface descriptors and attachment patterns, supported by established literature. At the nanoscale to sub-microscale, pili and curli fimbriae adapt their length and orientation to engage with nanorough or patterned surfaces, tethering into nanoscale pits and ridges and promoting irreversible attachment [82]. Appendage length further modulates in response to encountered features (flagella elongate on nanorough alumina, pili extend in thin silica wells, and both shorten in confined geometries) supporting active adaptation to surface architecture [83,84]. This fine-scale stabilization complements body–surface realignment on nanostructured substrates [83], collectively reducing detachment probability and biasing cells toward early clustering.

These nanoscale anchoring events carry upward into the microscale regime, where flagella probe and hook into ridges, hollows, and hummocks [85]. When features provide mechanical “hooks,” attachment persists; when they do not, reversible adhesion dominates and cells retain higher mobility [85]. Microscale valleys or depressions can also trap cells, limiting lateral encounters and delaying microcolony formation, depending on valley depth and peak-to-peak spacing [85].

These hierarchical mechanisms map directly onto our image-derived mesoscale metrics. Surfaces that, based on SEM, allowed closer packing or more continuous biofilm-like structures also showed increased area coverage and more frequent cluster formation (**Figure 8a** and **8e**). Conversely, surfaces with isolated or sparsely distributed bacteria corresponded to decreased coverage and fewer detected clusters (**Figure 8f** and **8h**). This agrees with the notion that once early attachment stabilizes, appendage entanglement and extracellular polymeric substances secretion reinforce cell immobilization and multicellular cohesion [86], making mesoscale clustering the cumulative expression of nanoscale tethering and microscale confinement.

3.2.2 Area Coverage and Colony Size Distributions Across Treatments

Area coverage measurements from SYTO 9 staining further support the qualitative trends and multiscale narrative. SF 45 displayed the largest covered surface area, followed by SF 60. SF consistently exhibited much higher biofilm coverage than Ch (**Figure 9d**). In Ch samples, Ch 45 showed greater area coverage than Ch Control, whereas Ch 60 showed minimal coverage (dropping from roughly 5% in the control to less than 1% in Ch 60), reflecting sparse colonization. In contrast, SF 60 increased area coverage from ~13% in the control to ~17%. Overall, within each material, the 45-degree samples exhibited the greatest area coverage, while the 60-degree samples decreased substantially toward control values, except for the noted increase in SF 60.

The size distribution for bacterial colonies was extremely right-skewed (**Supplementary Figure S2**), making summary statistics from the distribution challenging to interpret. Moreover, as discussed in the introduction, there is a strong scale-dependence to many observed surface-biology interactions [33,35,38]. Finally, individual bacteria themselves behave quite differently than biofilms [24,87], as isolated cells typically exhibit transient and reversible attachment, whereas clusters and biofilms represent progressively stabilized, multicellular assemblies whose formation reflects collective behavior across multiple length scales. These factors, combined with qualitative observations from SEM and fluorescence images, motivated the separation of bacterial structures by size. These size ranges were defined as 1-20 μm^2 , 20-200 μm^2 , and $> 200 \mu\text{m}^2$, shown in **Figure 9 a-c**.

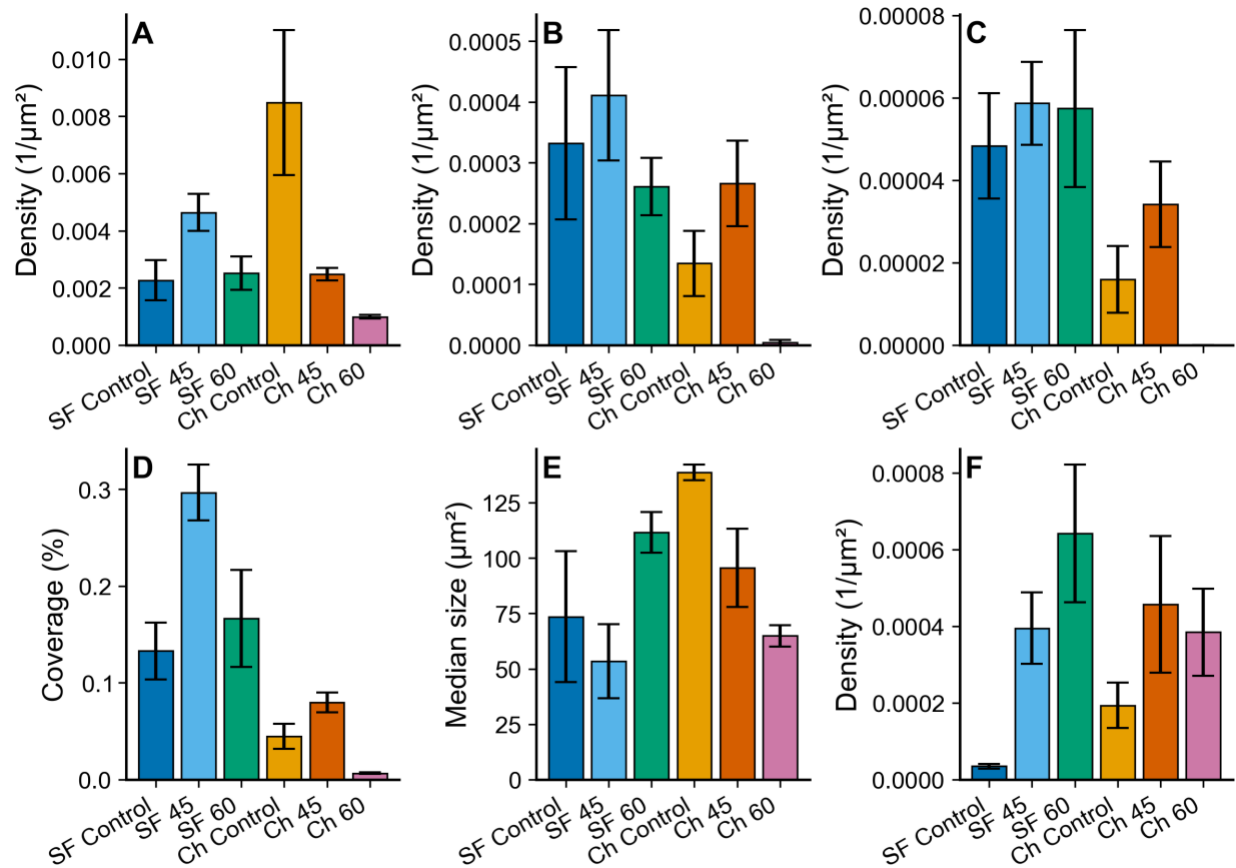


Figure 9. Biological response data across the six material-treatment groups. Each bar shown is the mean value across images along with standard error. These are descriptive, as images were not collected from independent samples. A) Area density of small (1-20 μm^2), B) medium (20-200 μm^2), and C) large ($>200 \mu\text{m}^2$) bacterial colonies. D) Fractional biofilm area coverage, E) median macrophage size (area), and F) macrophage area density.

Small (1-20 μm^2) colony density showed differing trends with respect to material and treatment; in the case of Ch films, small colony density continuously and sharply decreased from Ch Control to Ch 45, and to Ch 60, which exhibited the lowest number of small bacterial structures out of all the material-sample combinations. SF showed a much different trend: density increased from SF Control to SF 45 and then decreased slightly to SF 60 back to near the control value. Thus, DPNS treatment seemed to elicit a larger change in small colony density in Ch than in SF. The six groups displayed some differences in their mitigation of medium bacterial colonies compared to small bacterial colonies. For SF, medium colony density trended similarly to small colony density. In the Ch samples, while Ch 60 remained the least supportive of bacterial growth, Ch 45 supported more intermediate-sized clusters than Ch Control. Interestingly, Ch Control supported fewer medium

bacterial colonies than SF Control, despite supporting a much higher density of small colonies than SF Control, reflecting the qualitative observations of isolated clusters in Ch Control compared to the continuous films in SF Control.

The apparent gaps between material and treatment widened further when observing the number of large bacterial colonies supported on the material surfaces. Large bacterial colony density was effectively unchanged from control to treated SF. Of the Ch groups, Ch 45 supported the highest density of bacterial colonies while Ch 60 supported none. As with the medium colonies, Ch Control supported much fewer large bacterial colonies than SF Control. Collectively, the data indicated that treatment produced more marked changes in colony density in Ch across colony sizes than in SF. Treatment only seemed to impact the density of small bacteria in SF, and only marginally so. Moreover, Ch Control supported a high degree of isolated, small colonies, whereas SF Control was characterized instead by medium and large colonies.

Chitosan surfaces have been reported to be permissive to early bacterial contact, particularly when surface properties are modified in ways that favor adhesion. Under these conditions, chitosan's surface charge and mechanical compliance can enhance initial bacterial attachment, allowing bacteria to dock on the surface prior to subsequent stages such as biofilm maturation [88]. Importantly, early bacterial contact with a surface can be maintained even when progression toward mature biofilm formation is inhibited, a behavior often attributed to disrupted stabilization rather than reduced attachment frequency. In such cases, initial attachment may proceed normally, while later steps required for biofilm maturation, including extracellular polymeric substance production and multilayered cell accumulation, are impaired [89].

In contrast, multiple studies have reported that SF supports cohesive biofilm formation, even when initial bacterial attachment is comparatively limited. SF's moderate wettability and robust network structure, frequently associated with β -sheet-rich conformations, provide favorable conditions for bacterial adhesion and subsequent biofilm development. While initial attachment may still depend on specific surface properties and can be lower than on other substrates, once bacteria are present, SF promotes strong cell-cell interactions and biofilm cohesion, leading to the formation of mature and stable biofilm structures [90]. In this context, our results extend existing literature by demonstrating that these material-dependent behaviors emerge at distinct length scales: Ch surfaces exhibit a bottleneck between early attachment and cluster maturation that is highly sensitive to DPNS treatment, whereas SF surfaces maintain mesoscale organization that is comparatively robust to nanoscale modification.

3.2.3 Macrophage Response

To characterize macrophage adhesion behavior, we quantified the projected area of macrophage clusters formed on the different surface conditions. In this context, clusters were defined as spatially contiguous groups of adherent macrophages, representing localized regions of stabilized adhesion rather than isolated, highly motile cells. Macrophage attachment and clustering are mediated by dynamic cytoskeletal protrusions, including filopodia and lamellipodia, which actively probe the surface, establish adhesive contacts, and facilitate cell–cell interactions [91,92]. These appendage-like structures were qualitatively observed in SEM images as elongated protrusions extending from adherent macrophages and interacting with surface features. Unlike bacteria, whose dimensions are comparable to nanoscale surface features and can therefore be mechanically trapped or confined, macrophages operate at a much larger characteristic length scale (15–18 μm for j774 in spherical state [93]), passing over individual nanostructures and voids and instead integrating nanoscale cues through collective adhesion and spreading responses. Cluster area was therefore used as a mesoscale descriptor of collective cellular organization, integrating surface-mediated confinement and cell–cell proximity. While this analysis does not aim to infer macrophage activation state or fusion, it provides a quantitative framework to compare how multiscale surface properties influence the extent and organization of macrophage clustering.

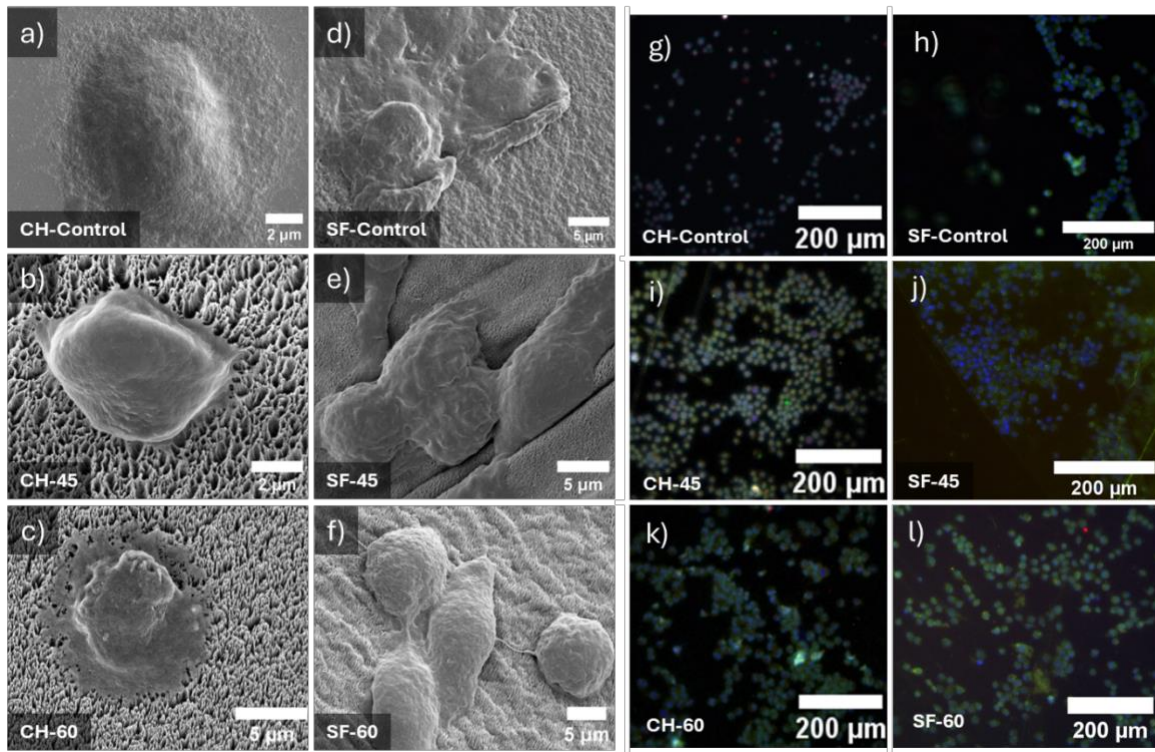


Figure 10. Representative macrophage adhesion and morphology on chitosan (Ch) and silk fibroin (SF) surfaces under different surface treatments. SEM images illustrate macrophage morphologies on chitosan surfaces: (a) Ch Control, (b) Ch 45, and (c) Ch 60, and on silk fibroin surfaces: (d) SF Control, (e) SF 45, and (f) SF 60. Fluorescence microscopy images show corresponding macrophage distributions and clustering behavior on (g) Ch Control, (i) Ch 45, and (k) Ch 60, and on (h) SF Control, (j) SF 45, and (l) SF 60, illustrating treatment-dependent differences in projected cell area, spatial distribution, and cluster formation at the population level. *Panels (d–f) were adapted from [10] with permission. Copyright © 2024 Elsevier.*

SEM observations were used to resolve macrophage adhesion and spreading behaviors at the local scale. Across the Ch surfaces, macrophage morphology was modulated by treatment. On Ch Control, macrophages appeared extensively spread with large projected contact areas, reflecting stable cell–surface interactions. Ch 45 surfaces supported macrophages with more compact morphologies and reduced spreading, indicative of attachment events that remain weakly stabilized. In contrast, Ch 60 exhibited more flattened macrophages with larger contact areas than Ch 45, suggesting enhanced cell-surface adhesion.

Median macrophage particle size showed different trends with respect to material and treatment. In the Ch samples, the median macrophage size decreased continuously from Ch Control to Ch 45 to Ch 60. In contrast, median macrophage size on SF was lowest for the 45-degree sample and highest for the 60-degree sample. Macrophage area density increased sharply with respect to treatment in SF. Together, the median particle size and area density data showed that Ch Control was characterized by fewer, larger clusters relative to Ch 45 and Ch 60, which a higher density of smaller, isolated macrophages. The data for SF showed that SF control had a low area density of intermediate-sized particles, SF 45 supported intermediate macrophage density and size, and SF 60 had many large particles, indicating that irradiation of SF promoted macrophage attachment and spreading.

3.3 Correlation of Biological Data with Surface Properties

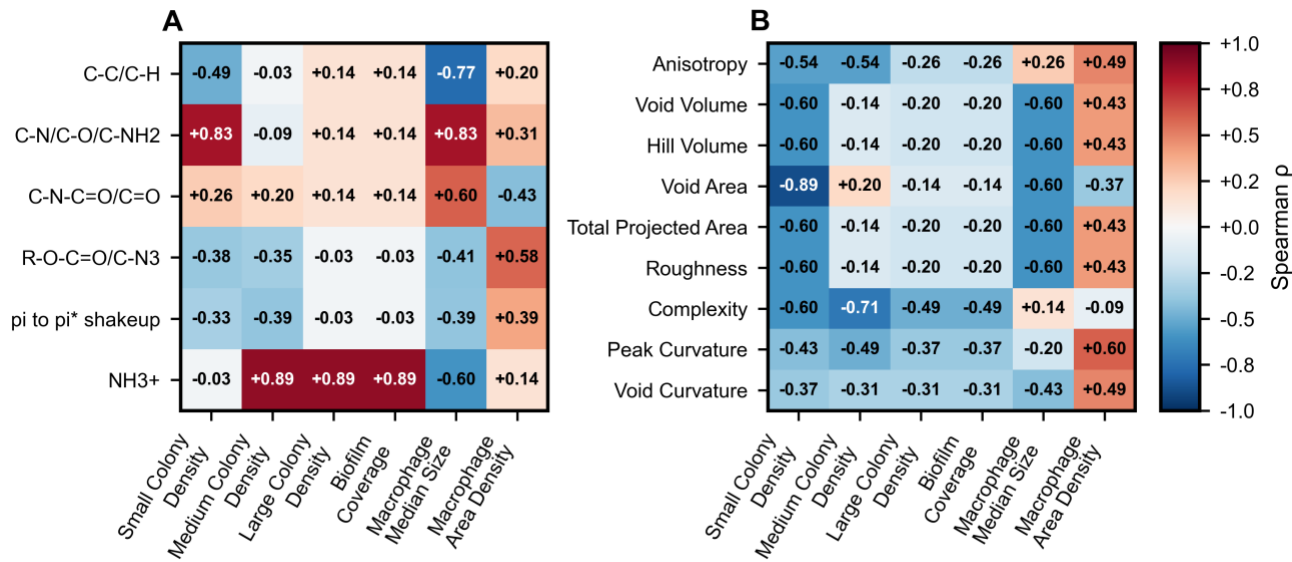


Figure 11. Heat maps of chemistry and single-scale topographic data with biological data.

A) Functional group heat map and B) single-scale topography heat map.

3.3.1 Surface Chemistry:

Although irradiation-induced chemical modifications are typically confined to the outermost nanometers of the surface [10], this region defines the biologically active interface governing protein adsorption and initial adhesion events. Near-surface chemical functionalities regulate charge distribution, hydration, and short-range interactions, which collectively determine the composition and conformation of the adsorbed protein layer that mediates subsequent biological contact [94]. As a result, chemical variations restricted to the first few nanometers can propagate upward to influence collective biological organization, linking near-surface chemistry to multiscale adhesion behavior.

Data associated with larger bacterial colonies and surface-associated structures (large and medium colony density and biofilm coverage) showed a strong positive correlation with NH_3^+ concentration, whereas correlations with other functional groups were comparatively weak (**Figure 11 A**). Because NH_3^+ levels were consistently higher on SF than on Ch, this correlation may partially reflect material-specific chemistry rather than an isolated functional-group effect. Previous reports indicate that protonated amines confer a net positive charge to the near-surface region, which may favor electrostatic interactions with the negatively charged bacterial envelope characteristic of *E. coli* [95,96]. Such interactions are consistent with increased stabilization of

bacterial attachment and the emergence of larger bacterial assemblies, without implying a direct causal relationship.

In contrast, small bacterial colonies and isolated bacteria correlated with C–C/C–O/C–NH₂ concentration and showed a moderate negative relationship with C–C/C–H, but no evident association with protonated amines. These neutral or weak polar groups are typically linked to short-range interactions rather than long-range electrostatic forces, aligning with attachment behaviors that remain weakly stabilized and spatially limited [97,98].

J774 macrophages exhibited broader and stronger correlations with surface chemistry than bacteria, consistent with their mode of surface sensing. Unlike bacteria, which interact with substrates primarily through localized, appendage-mediated contacts, macrophages integrate interfacial cues over large contact areas through active spreading and cytoskeletal reorganization. It has been shown that J774 macrophages actively regulate their apparent surface area via cortical tension modulation and actin remodeling, enabling surface integration across micrometer-length scales [93,99]. This capacity for large-scale deformation allows macrophages to integrate both chemical and topological cues, rather than responding to chemistry alone.

In this context, macrophage median size showed a high correlation with C–C/C–O/C–NH₂ concentration, a moderate positive correlation with C–N–C=O/C=O concentration, and negative correlations with C–C/C–H and NH₃⁺ groups, suggesting an association between surface chemistry and macrophage spreading and projected contact area, rather than simple attachment. Moreover, macrophage area density exhibited a moderate positive correlation with R–O–C=O/C–N₃ functionalities, suggesting chemistry-dependent differences in cell clustering. Neutral or moderately polar surface chemistries have been shown to promote selective adsorption and preserved bioactivity of serum proteins, thereby defining the biological identity of the interface and regulating macrophage interactions through integrin-mediated pathways [100].

3.3.2 Single-Scale Topography

Single scale topography data (**Figure 11b**) mirrored general results of the chemistry data. Broadly speaking, small bacterial structures and macrophages again showed strong correlation over a broad range of parameters, indicating a more robust link with surface properties and, by extension, material/treatment. Moreover, topographic parameters associated with roughness, complexity, volume, and area were closely related, as indicated by the similar correlation strengths of those families. Medium bacterial colony density showed correlation with only anisotropy and peak curvature while large bacterial colonies and area coverage showed weak correlation with all

topographic parameters, indicating decreasing correlation strength with increasing colony size. Macrophage median size again showed stronger overall correlation with surface properties than macrophage area density, exhibiting a moderate negative correlation across volume, area, and roughness-associated parameters. Macrophage area density, on the other hand, correlated more strongly with complexity, curvature, and anisotropy.

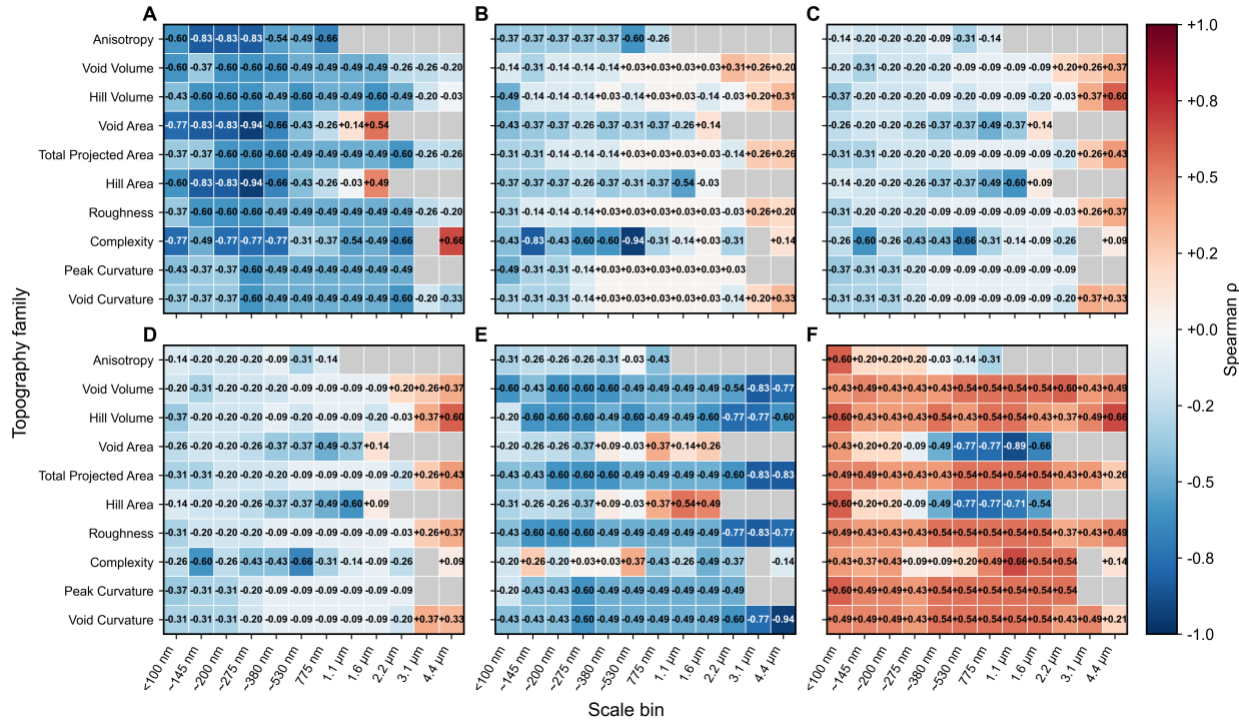


Figure 12: Heat maps of multiscale topographic data with biological data. A) Small colony density, B) medium colony density, C) large colony density, D) biofilm coverage, E) median macrophage size, and F) macrophage area density.

3.3.3 Multiscale Topography: Bandpass Data

Multiscale topography data offered deeper insight into the scale-dependence of correlations in the biological data. Interestingly, broad relationships between the scale of biological features and the scale of observation which showed the strongest correlation could be observed. Small colony density showed the strongest and broadest correlation with bandpass data, including parameters associated with volume, area, roughness, anisotropy, and complexity, reinforcing the single-scale results. Importantly, bandpass data showed an increase in correlation strength at smaller scales, near 145-380 nm, and a strong decrease in correlation strength at larger scales, suggesting a scale-dependent relationship between surface topography and small colony density. Given the

stronger topographic changes in treated Ch in the 145-380 nm range, it is plausible that nanostructuring at this scale contributed to mitigation of bacterial attachment and proliferation, which is supported by the earlier SEM analysis. Void/hill areas, complexity, and anisotropy correlated particularly strongly as opposed to peak curvature, suggesting this mitigation was likely not due to rupturing of the cell wall by nano “spikes” as observed in some bactericidal topographies [25,34], but rather due to trapping or prevention of adhesion, as observed in the SEM images.

Larger bacterial structures generally showed much lower correlation with topographic parameters aside from complexity, which was negatively correlated with large and medium colony density. Importantly, the scale of maximum correlation was roughly 500 nm – 1.1 μm , slightly larger than that for small bacterial colonies, and was stronger for medium colony density than for large colony density, again indicating a decrease in correlation between colony response and surface conditions as the size of the colony increased. The density of medium and large structures was notably higher in SF than in Ch, irrespective of treatment. These structures were positively correlated with NH_3^+ concentration, which was highest in SF, though with very low (< 3 at%) overall abundance (**Figure S2**). Thus, NH_3^+ was likely a proxy for material classification rather than a causal agent. Ch 60 consistently exhibited the lowest density of bacterial colonies, independent of colony size.

These data indicate a complex, size- and material-dependent relationship wherein topography alone has decreasing correlation strength with increasing colony size. Topography exerted a weakening impact on larger bacterial structures in SF, whereas treated Ch mitigated these structures readily, and with increasing ability as topography became more pronounced. Thus, the efficacy of the tested topography in mitigating biofilm formation is likely contingent on both the size of the colony as well as intrinsic material properties. Given the generally weak correlation of large colonies with the collected data, it is likely that testing combination effects or higher-level properties (e.g., wettability, surface charge) is necessary to accurately assess material performance in this regard.

As with the single-scale data, macrophage data correlated strongly with multiscale topography. Macrophage median size exhibited broad negative correlation with volume, area, and roughness and strong negative correlation with void curvature. These correlation strengths were highest at the absolute largest scales of measurement, from 2.2 – 4.1 μm . Interestingly, these data contrast that for macrophage area density, which essentially correlate in the inverse direction and with stronger correlation at intermediate scales, near 500 nm – 1.6 μm . These data showed the

strongest correlation with void and hill areas. Void and hill area show differing signs in their correlations with respect to scale in both macrophage datasets, indicating a reversal in the trend of hill and void areas as scale decreases (**Supplementary Figure S5**).

4. Conclusions and Outlook

Multiscale analysis techniques were employed to investigate the surface properties of DPNS-treated SF and Ch films and their relationship with biological responses relevant to wound healing. DPNS produced multiscale topographic alterations to both Ch and SF along with surface carbonization, deoxygenation, and changes in nitrogen chemistry, with topographic changes being more pronounced in Ch than SF.

Biofilm formation was far more hindered on treated Ch than on SF, reflecting the differential impact of the treated surfaces on large bacterial structures. Multiscale data revealed scale-dependence in biological interactions with surface topography; individual bacteria and small colonies were strongly negatively correlated with small-scale topography, whereas correlation strength weakened as bacterial colony size increased, indicating a complex relationship between large colony behavior and surface properties that could not be captured by the individual topographic or chemical parameters measured. In contrast, macrophage responses correlated most strongly with larger scale surface features, reflecting their larger size and integrated adhesion and spreading behavior. Opposing trends in cluster size and area density across scale indicate that surface features regulate both macrophage spreading and spatial organization. The above clearly demonstrates that scale is a relevant factor in understanding the role of topography in impacting biological response.

These findings extend our understanding of the impact of surface properties on materials by highlighting scale as a potential design parameter for wound-healing materials, wherein feature size could be tailored to the characteristic scale length of the target biological structure. Multiscale alterations mitigate biofilm formation without cytotoxicity, particularly in Ch films, likely due to trapping interrupted attachment as opposed to bactericidal mechanisms. The inability of DPNS-treated SF to prevent biofilm formation suggests the need for combinatorial approaches (i.e., leveraging surface charge and inherent antimicrobial properties in addition to topography) to maximize the efficacy of topography in mitigating biofilm formation.

The introduction of two multiscale analysis techniques in biomaterials characterization and analysis provides a framework for scale-aware, quantitative analysis of complex biomaterial surfaces. Bandpass filtration captured a wider variety of topographic parameters than the

multiscale curvature tensor method and thus was generally better able to capture correlations with biological response. A key aspect of this study was the comparison of multiscale analysis techniques to conventional or single-scale methods. Though single-scale methods could characterize key topographic features and associated correlations, multiscale methods demonstrated stronger correlations, were better able to discriminate surfaces, and, most importantly, could ascribe to these specific scales, enabling a more detailed analysis of the material performance and the impact of DPNS treatment.

A limitation in the present work was limited sample size compared to the parameter space (i.e., $n \ll p$). Further studies should collect more data to improve statistical power, particularly for multiscale data, allowing direct interpretation of the key surface features and scales driving biological response. Due to the extreme multicollinearity in multiscale data, efforts to cluster or prune data prior to analysis are recommended. Partial Least Squares (PLS) regression is a viable statistical framework to infer causality in this context if sample size is sufficiently large [101–103]. Additionally, broadening the set of characterization parameters to include surface charge and wettability and/or allowing interaction between factors in statistical modelling would allow more comprehensive characterization data and analysis. Finally, given the importance of protein adhesion in dictating subsequent cell attachment and behavior, direct investigation of protein adhesion via multiscale analysis could provide clearer mechanistic connections between surface properties and performance.

5. Acknowledgement

The authors acknowledge the Materials Research Institute (MRI) at Penn State for access to shared instrumentation, as well as technical training and expert support, including use of the Thermo Scientific Verios G4 scanning electron microscope (SEM), Thermo Scientific Scios FIB-SEM, Physical Electronics VersaProbe III X-ray photoelectron spectrometer (XPS), and Bruker Icon Dimension II atomic force microscope (AFM).

5.1.1 Declaration of generative AI and AI-assisted technologies in the manuscript preparation process

During the preparation of this work, the authors used artificial intelligence-assisted tools, including ChatGPT, Perplexity, and Gemini in order to help write code for parsing, analyzing, and plotting

data. After using this tool/service, the authors reviewed and edited the content as needed and take full responsibility for the content of this published article.

6. Supporting Information

Supporting information: Single-scale topographic data, bacterial colony size distributions, functional group abundances, multiscale curvature tensor heat maps, multiscale data relative scores, and topographic family designations and ISO definitions (DOCX).

7. References

- [1] Järbrink K, Ni G, Sönnergren H, Schmidtchen A, Pang C, Bajpai R, et al. Prevalence and incidence of chronic wounds and related complications: a protocol for a systematic review. *Systematic Reviews* 2016;5:152. <https://doi.org/10.1186/s13643-016-0329-y>.
- [2] Popescu V, Cauni V, Petruțescu MS, Rustin MM, Bocai R, Turculeț CR, et al. Chronic Wound Management: From Gauze to Homologous Cellular Matrix. *Biomedicines* 2023;11:2457. <https://doi.org/10.3390/biomedicines11092457>.
- [3] Percival SL, Hill KE, Williams DW, Hooper SJ, Thomas DW, Costerton JW. A review of the scientific evidence for biofilms in wounds. *Wound Repair and Regeneration* 2012;20:647–57. <https://doi.org/10.1111/j.1524-475X.2012.00836.x>.
- [4] Wolcott R d., Rhoads D d., Dowd S e. Biofilms and chronic wound inflammation. *J Wound Care* 2008;17:333–41. <https://doi.org/10.12968/jowc.2008.17.8.30796>.
- [5] Chouhan D, Mandal BB. Silk biomaterials in wound healing and skin regeneration therapeutics: From bench to bedside. *Acta Biomaterialia* 2020;103:24–51. <https://doi.org/10.1016/j.actbio.2019.11.050>.
- [6] dos Santos FV, Siqueira RL, de Moraes Ramos L, Yoshioka SA, Branciforti MC, Correa DS. Silk fibroin-derived electrospun materials for biomedical applications: A review. *International Journal of Biological Macromolecules* 2024;254:127641. <https://doi.org/10.1016/j.ijbiomac.2023.127641>.
- [7] Fazal T, Murtaza BN, Shah M, Iqbal S, Rehman M, Jaber F, et al. Recent developments in natural biopolymer based drug delivery systems. *RSC Adv* n.d.;13:23087–121. <https://doi.org/10.1039/d3ra03369d>.
- [8] Ghalei S, Handa H. A review on antibacterial silk fibroin-based biomaterials: current state and prospects. *Materials Today Chemistry* 2022;23:100673. <https://doi.org/10.1016/j.mtchem.2021.100673>.
- [9] González-Restrepo D, Zuluaga-Vélez A, Orozco LM, Sepúlveda-Arias JC. Silk fibroin-based dressings with antibacterial and anti-inflammatory properties. *European Journal of Pharmaceutical Sciences* 2024;195:106710. <https://doi.org/10.1016/j.ejps.2024.106710>.

- [10] Posada VM, Marin A, Mesa-Restrepo A, Nashed J, Allain JP. Enhancing silk fibroin structures and applications through angle-dependent Ar+ plasma treatment. *International Journal of Biological Macromolecules* 2024;257:128352. <https://doi.org/10.1016/j.ijbiomac.2023.128352>.
- [11] Qi Y, Wang H, Wei K, Yang Y, Zheng R-Y, Kim IS, et al. A Review of Structure Construction of Silk Fibroin Biomaterials from Single Structures to Multi-Level Structures. *Int J Mol Sci* 2017;18:237. <https://doi.org/10.3390/ijms18030237>.
- [12] Yan D, Li Y, Liu Y, Li N, Zhang X, Yan C. Antimicrobial Properties of Chitosan and Chitosan Derivatives in the Treatment of Enteric Infections. *Molecules* 2021;26:7136. <https://doi.org/10.3390/molecules26237136>.
- [13] Liu H, Wang C, Li C, Qin Y, Wang Z, Yang F, et al. A functional chitosan-based hydrogel as a wound dressing and drug delivery system in the treatment of wound healing. *RSC Adv* 2018;8:7533–49. <https://doi.org/10.1039/C7RA13510F>.
- [14] Matica MA, Aachmann FL, Tøndervik A, Sletta H, Ostafe V. Chitosan as a Wound Dressing Starting Material: Antimicrobial Properties and Mode of Action. *International Journal of Molecular Sciences* 2019;20:5889. <https://doi.org/10.3390/ijms20235889>.
- [15] Sahariah P, Másson M. Antimicrobial Chitosan and Chitosan Derivatives: A Review of the Structure–Activity Relationship. *Biomacromolecules* 2017;18:3846–68. <https://doi.org/10.1021/acs.biomac.7b01058>.
- [16] Guarnieri A, Triunfo M, Scieuzo C, Ianniciello D, Tafi E, Hahn T, et al. Antimicrobial properties of chitosan from different developmental stages of the bioconverter insect *Hermetia illucens*. *Sci Rep* 2022;12:8084. <https://doi.org/10.1038/s41598-022-12150-3>.
- [17] Kong M, Chen XG, Xing K, Park HJ. Antimicrobial properties of chitosan and mode of action: A state of the art review. *International Journal of Food Microbiology* 2010;144:51–63. <https://doi.org/10.1016/j.ijfoodmicro.2010.09.012>.
- [18] Silva SS, Luna SM, Gomes ME, Benesch J, Pashkuleva I, Mano JF, et al. Plasma Surface Modification of Chitosan Membranes: Characterization and Preliminary Cell Response Studies. *Macromolecular Bioscience* 2008;8:568–76. <https://doi.org/10.1002/mabi.200700264>.
- [19] Jaramillo-Correa C, Posada VM, Nashed J, Civantos A, Allain JP. Analysis of Antibacterial Efficacy and Cellular Alignment Regulation on Plasma Nanotextured Chitosan Surfaces. *Langmuir* 2023;39:14573–85. <https://doi.org/10.1021/acs.langmuir.3c01808>.
- [20] Bandara CD, Singh S, Afara IO, Wolff A, Tesfamichael T, Ostrikov K, et al. Bactericidal Effects of Natural Nanotopography of Dragonfly Wing on *Escherichia coli*. *ACS Appl Mater Interfaces* 2017;9:6746–60. <https://doi.org/10.1021/acsami.6b13666>.
- [21] Ivanova EP, Hasan J, Webb HK, Truong VK, Watson GS, Watson JA, et al. Natural bactericidal surfaces: mechanical rupture of *Pseudomonas aeruginosa* cells by cicada wings. *Small* 2012;8:2489–94. <https://doi.org/10.1002/smll.201200528>.

- [22] Watson GS, Green DW, Schwarzkopf L, Li X, Cribb BW, Myhra S, et al. A gecko skin micro/nano structure – A low adhesion, superhydrophobic, anti-wetting, self-cleaning, biocompatible, antibacterial surface. *Acta Biomaterialia* 2015;21:109–22. <https://doi.org/10.1016/j.actbio.2015.03.007>.
- [23] Linklater DP, Juodkazis S, Rubanov S, Ivanova EP. Comment on “Bactericidal Effects of Natural Nanotopography of Dragonfly Wing on Escherichia coli.” *ACS Appl Mater Interfaces* 2017;9:29387–93. <https://doi.org/10.1021/acsami.7b05707>.
- [24] Khatoon Z, McTiernan CD, Suuronen EJ, Mah T-F, Alarcon EI. Bacterial biofilm formation on implantable devices and approaches to its treatment and prevention. *Helijon* 2018;4:e01067. <https://doi.org/10.1016/j.heliyon.2018.e01067>.
- [25] Modaresifar K, Azizian S, Ganjian M, Fratila-Apachitei LE, Zadpoor AA. Bactericidal effects of nanopatterns: A systematic review. *Acta Biomaterialia* 2019;83:29–36. <https://doi.org/10.1016/j.actbio.2018.09.059>.
- [26] Arias SL, Cheng MK, Civantos A, Devorkin J, Jaramillo C, Allain JP. Ion-Induced Nanopatterning of Bacterial Cellulose Hydrogels for Biosensing and Anti-Biofouling Interfaces. *ACS Appl Nano Mater* 2020;3:6719–28. <https://doi.org/10.1021/acsanm.0c01151>.
- [27] Arias SL, Devorkin J, Spear JC, Civantos A, Allain JP. Bacterial Envelope Damage Inflicted by Bioinspired Nanostructures Grown in a Hydrogel. *ACS Appl Bio Mater* 2020;3:7974–88. <https://doi.org/10.1021/acsabm.0c01076>.
- [28] Mesa-Restrepo A, Byers E, Brown JL, Ramirez J, Allain JP, Posada VM. Osteointegration of Ti Bone Implants: A Study on How Surface Parameters Control the Foreign Body Response. *ACS Biomater Sci Eng* 2024;10:4662–81. <https://doi.org/10.1021/acsbiomaterials.4c00114>.
- [29] Aditya T, Mesa-Restrepo A, Civantos A, Cheng M-K, Jaramillo-Correa C, Posada VM, et al. Ion Bombardment-Induced Nanoarchitectonics on Polyetheretherketone Surfaces for Enhanced Nanoporous Bioactive Implants. *ACS Appl Bio Mater* 2023;6:4922–34. <https://doi.org/10.1021/acsabm.3c00642>.
- [30] Posada VM, Ramírez J, Civantos A, Fernández-Morales P, Allain JP. Ion-bombardment-driven surface modification of porous magnesium scaffolds: Enhancing biocompatibility and osteoimmunomodulation. *Colloids and Surfaces B: Biointerfaces* 2024;234:113717. <https://doi.org/10.1016/j.colsurfb.2023.113717>.
- [31] Posada VM, Civantos A, Ramírez J, Fernández-Morales P, Allain JP. Tailoring adaptive bioresorbable Mg-based scaffolds with directed plasma nanosynthesis for enhanced osseointegration and tunable resorption. *Applied Surface Science* 2021;550:149388. <https://doi.org/10.1016/j.apsusc.2021.149388>.
- [32] Anselme K, Davidson P, Popa AM, Giazzon M, Liley M, Ploux L. The interaction of cells and bacteria with surfaces structured at the nanometre scale. *Acta Biomaterialia* 2010;6:3824–46. <https://doi.org/10.1016/j.actbio.2010.04.001>.

- [33] Gu H, Chen A, Song X, Brasch ME, Henderson JH, Ren D. How *Escherichia coli* lands and forms cell clusters on a surface: A new role of surface topography. *Scientific Reports* 2016;6. <https://doi.org/10.1038/srep29516>.
- [34] Mirzaali MJ, van Dongen ICP, Tümer N, Weinans H, Yavari SA, Zadpoor AA. In-silico quest for bactericidal but non-cytotoxic nanopatterns. *Nanotechnology* 2018;29:43LT02. <https://doi.org/10.1088/1361-6528/aad9bf>.
- [35] Wang Y, Subbiahdoss G, Swartjes J, van der Mei HC, Busscher HJ, Libera M. Length-Scale Mediated Differential Adhesion of Mammalian Cells and Microbes. *Advanced Functional Materials* 2011;21:3916–23. <https://doi.org/10.1002/adfm.201100659>.
- [36] Franz S, Rammelt S, Scharnweber D, Simon JC. Immune responses to implants – A review of the implications for the design of immunomodulatory biomaterials. *Biomaterials* 2011;32:6692–709. <https://doi.org/10.1016/j.biomaterials.2011.05.078>.
- [37] Luo J, Walker M, Xiao Y, Donnelly H, Dalby MJ, Salmeron-Sanchez M. The influence of nanotopography on cell behaviour through interactions with the extracellular matrix – A review. *Bioactive Materials* 2022;15:145–59. <https://doi.org/10.1016/j.bioactmat.2021.11.024>.
- [38] Lord MS, Foss M, Besenbacher F. Influence of nanoscale surface topography on protein adsorption and cellular response. *Nano Today* 2010;5:66–78. <https://doi.org/10.1016/j.nantod.2010.01.001>.
- [39] Kasemo B. Biological surface science. *Surface Science* 2002;500:656–77. [https://doi.org/10.1016/S0039-6028\(01\)01809-X](https://doi.org/10.1016/S0039-6028(01)01809-X).
- [40] Brown CA, Hansen HN, Jiang XJ, Blateyron F, Berglund J, Senin N, et al. Multiscale analyses and characterizations of surface topographies. *CIRP Annals* 2018;67:839–62. <https://doi.org/10.1016/j.cirp.2018.06.001>.
- [41] Bartkowiak T, Peta K, Królczyk J, Niesłony P, Bogdan-Chudy M, Przeszłowski Ł, et al. Wetting properties of polymer additively manufactured surfaces – Multiscale and multi-technique study into the surface-measurement-function interactions. *Tribology International* 2024;202:110394. <https://doi.org/10.1016/j.triboint.2024.110394>.
- [42] Chauvy PF, Madore C, Landolt D. Variable length scale analysis of surface topography: characterization of titanium surfaces for biomedical applications. *Surface and Coatings Technology* 1998;110:48–56. [https://doi.org/10.1016/S0257-8972\(98\)00608-2](https://doi.org/10.1016/S0257-8972(98)00608-2).
- [43] Dumas V, Guignandon A, Vico L, Mauclair C, Zapata X, Linossier MT, et al. Femtosecond laser nano/micro patterning of titanium influences mesenchymal stem cell adhesion and commitment. *Biomed Mater* 2015;10:055002. <https://doi.org/10.1088/1748-6041/10/5/055002>.
- [44] Gambardella A, Marchiori G, Maglio M, Russo A, Rossi C, Visani A, et al. Determination of the Spatial Anisotropy of the Surface MicroStructures of Different Implant Materials: An Atomic Force Microscopy Study. *Materials* 2021;14:4803. <https://doi.org/10.3390/ma14174803>.

[45] Watari S, Hayashi K, Wood JA, Russell P, Nealey PF, Murphy CJ, et al. Modulation of osteogenic differentiation in hMSCs cells by submicron topographically-patterned ridges and grooves. *Biomaterials* 2012;33:128–36. <https://doi.org/10.1016/j.biomaterials.2011.09.058>.

[46] Zink C, Hall H, Brunette DM, Spencer ND. Orthogonal nanometer-micrometer roughness gradients probe morphological influences on cell behavior. *Biomaterials* 2012;33:8055–61. <https://doi.org/10.1016/j.biomaterials.2012.07.037>.

[47] Peta K, Bartkowiak T, Rybicki M, Galek P, Mendak M, Wieczorowski M, et al. Scale-dependent wetting behavior of bioinspired lubricants on electrical discharge machined Ti6Al4V surfaces. *Tribology International* 2024;194:109562. <https://doi.org/10.1016/j.triboint.2024.109562>.

[48] Bartkowiak T, Berglund J, Brown CA. Multiscale Characterizations of Surface Anisotropies. *Materials (Basel)* 2020;13:3028. <https://doi.org/10.3390/ma13133028>.

[49] Berglund J, Wiklund D, Rosén B-G. A method for visualization of surface texture anisotropy in different scales of observation. *Scanning* 2011;33:325–31. <https://doi.org/10.1002/sca.20249>.

[50] Chen Q, Wang Y, Zhou J, Wu Y, Song H. Research on characterization of anisotropic and isotropic processing surfaces by characteristic roughness. *Journal of Materials Processing Technology* 2020;275:116277. <https://doi.org/10.1016/j.jmatprotec.2019.116277>.

[51] Iyer A, Dulal R, Zhang Y, Ghumman UF, Chien T, Balasubramanian G, et al. Designing anisotropic microstructures with spectral density function. *Computational Materials Science* 2020;179:109559. <https://doi.org/10.1016/j.commatsci.2020.109559>.

[52] Jana S, Levengood SKL, Zhang M. Anisotropic Materials for Skeletal-Muscle-Tissue Engineering. *Adv Mater* 2016;28:10588–612. <https://doi.org/10.1002/adma.201600240>.

[53] Leclech C, Villard C. Cellular and Subcellular Contact Guidance on Microfabricated Substrates. *Front Bioeng Biotechnol* 2020;8:551505. <https://doi.org/10.3389/fbioe.2020.551505>.

[54] Berglund J, Agunwamba C, Powers B, Brown CA, Rosén B -G. On discovering relevant scales in surface roughness measurement—an evaluation of a band-pass method. *Scanning* 2010;32:244–9. <https://doi.org/10.1002/sca.20168>.

[55] Brown CA, Blateyron F, Berglund J, Murison AJ, Jeswiet JJ. Spatial frequency decomposition with bandpass filters for multiscale analyses and functional correlations. *Surf Topogr: Metrol Prop* 2024;12:035031. <https://doi.org/10.1088/2051-672X/ad6f2f>.

[56] Rockwood DN, Preda RC, Yücel T, Wang X, Lovett ML, Kaplan DL. Materials fabrication from *Bombyx mori* silk fibroin. *Nat Protoc* 2011;6:1612–31. <https://doi.org/10.1038/nprot.2011.379>.

[57] George GA. High resolution XPS of organic polymers—the scienta ESCA 300 data base. G. Beamson and D. Briggs. John Wiley & Sons, Ltd, Chichester, 1992. Pp. 295, price £65.00.

ISBN 0-471-93592-1. *Polymer International* 1994;33:439–40.
<https://doi.org/10.1002/pi.1994.210330424>.

[58] Berkmans, F., Bartkowiak, T., Grochalski, K., Wieczorowski, M., & Bigerelle, M. Curvature-Based Multiscale Feature Extraction for Surface Quality Inspection in Manufacturing. *The International Journal of Advanced Manufacturing Technology* 2025. <https://doi.org/10.1007/s00170-025-17145-8>.

[59] Sung CH (Joseph), Hao T, Fang H, Nguyen AT, Perricone V, Yu H, et al. Biological and Biologically Inspired Functional Nanostructures: Insights into Structural, Optical, Thermal, and Sensing Applications. *Advanced Materials* n.d.;n/a:e09281.
<https://doi.org/10.1002/adma.202509281>.

[60] Xu X, Jia J, Guo M. The Most Recent Advances in the Application of Nano-Structures/Nano-Materials for Single-Cell Sampling. *Front Chem* 2020;8.
<https://doi.org/10.3389/fchem.2020.00718>.

[61] Gogolides E, Constantoudis V, Kokkoris G, Kontziamasis D, Tsougeni K, Boulousis G, et al. Controlling roughness: from etching to nanotexturing and plasma-directed organization on organic and inorganic materials. *J Phys D: Appl Phys* 2011;44:174021.
<https://doi.org/10.1088/0022-3727/44/17/174021>.

[62] Young KD. The Selective Value of Bacterial Shape. *Microbiology and Molecular Biology Reviews* 2006;70:660–703. <https://doi.org/10.1128/mmbr.00001-06>.

[63] Westfall CS, Levin PA. Bacterial Cell Size: Multifactorial and Multifaceted. *Annu Rev Microbiol* 2017;71:499–517. <https://doi.org/10.1146/annurev-micro-090816-093803>.

[64] Matienzo LJ, Winnacker SK. Dry Processes for Surface Modification of a Biopolymer: Chitosan. *Macromolecular Materials and Engineering* 2002;287:871–80.
<https://doi.org/10.1002/mame.200290022>.

[65] Maachou H, Genet MJ, Aliouche D, Dupont-Gillain CC, Rouxhet PG. XPS analysis of chitosan–hydroxyapatite biomaterials: from elements to compounds. *Surface and Interface Analysis* 2013;45:1088–97. <https://doi.org/10.1002/sia.5229>.

[66] Stevens JS, Luca ACD, Pelendritis M, Terenghi G, Downes S, Schroeder SLM. Quantitative analysis of complex amino acids and RGD peptides by X-ray photoelectron spectroscopy (XPS). *Surface and Interface Analysis* 2013;45:1238–46. <https://doi.org/10.1002/sia.5261>.

[67] Lawrie G, Keen I, Drew B, Chandler-Temple A, Rintoul L, Fredericks P, et al. Interactions between Alginate and Chitosan Biopolymers Characterized Using FTIR and XPS. *Biomacromolecules* 2007;8:2533–41. <https://doi.org/10.1021/bm070014y>.

[68] Kurmaev EZ, Shin S, Watanabe M, Eguchi R, Ishiwata Y, Takeuchi T, et al. Probing oxygen and nitrogen bonding sites in chitosan by X-ray emission. *Journal of Electron Spectroscopy and Related Phenomena* 2002;125:133–8. [https://doi.org/10.1016/S0368-2048\(02\)00094-4](https://doi.org/10.1016/S0368-2048(02)00094-4).

[69] Wang Z, Sun C, Vigesna G, Liu H, Liu Y, Li J, et al. Glycosylated aniline polymer sensor: Amine to imine conversion on protein–carbohydrate binding. *Biosensors and Bioelectronics* 2013;46:183–9. <https://doi.org/10.1016/j.bios.2013.02.030>.

[70] Liu Y, Liu Y, Park M, Park SJ, Zhang Y, Akanda MR, et al. Green synthesis of fluorescent carbon dots from carrot juice for in vitro cellular imaging. *Carbon Letters* 2017;21:61–7. <https://doi.org/10.5714/CL.2017.21.061>.

[71] Maerten C, Garnier T, Lupattelli P, Chau NTT, Schaaf P, Jierry L, et al. Morphogen Electrochemically Triggered Self-Construction of Polymeric Films Based on Mussel-Inspired Chemistry. *Langmuir* 2015;31:13385–93. <https://doi.org/10.1021/acs.langmuir.5b03774>.

[72] Ando RA, Nascimento GMD, Landers R, Santos PS. Spectroscopic investigation of conjugated polymers derived from nitroanilines. *Spectrochimica Acta Part A: Molecular and Biomolecular Spectroscopy* 2008;69:319–26. <https://doi.org/10.1016/j.saa.2007.03.046>.

[73] Stevens JS, Schroeder SLM. X-Ray Photoelectron Spectroscopy. *Encyclopedia of Physical Organic Chemistry*, John Wiley & Sons, Ltd; 2017, p. 1–53. <https://doi.org/10.1002/9781118468586.epoc4031>.

[74] Prabhuram J, Wang X, Hui CL, Hsing IM. Synthesis and characterization of surfactant-stabilized Pt/C nanocatalysts for fuel cell applications. *Journal of Physical Chemistry B* 2003;107:11057–64. <https://doi.org/10.1021/jp0357929>.

[75] Takeuchi M, Shimizu Y, Yamagawa H, Nakamuro T, Anpo M. Preparation of the visible light responsive N3–doped WO₃ photocatalyst by a thermal decomposition of ammonium paratungstate. *Applied Catalysis B: Environmental* 2011;110:1–5. <https://doi.org/10.1016/j.apcatb.2011.08.004>.

[76] Remy MJ, Genet MJ, Lardinois PF, Notté PP, Poncelet G. Acidity of the outer surface of dealuminated mordenites as studied by X-ray photoelectron spectroscopy of chemisorbed ammonia. *Surface and Interface Analysis* 1994;21:643–9. <https://doi.org/10.1002/sia.740210908>.

[77] Simon-Walker R, Romero R, Staver JM, Zang Y, Reynolds MM, Popat KC, et al. Glycocalyx-Inspired Nitric Oxide-Releasing Surfaces Reduce Platelet Adhesion and Activation on Titanium. *ACS Biomater Sci Eng* 2017;3:68–77. <https://doi.org/10.1021/acsbiomaterials.6b00572>.

[78] Amornsudthiwat P, Mongkolnavin R, Kanokpanont S, Panpranot J, Wong CS, Damrongsakkul S. Improvement of early cell adhesion on Thai silk fibroin surface by low energy plasma. *Colloids and Surfaces B: Biointerfaces* 2013;111:579–86. <https://doi.org/10.1016/j.colsurfb.2013.07.009>.

[79] Jedlicka SS, Rickus JL, Zemlyanov DY. Surface Analysis by X-ray Photoelectron Spectroscopy of Sol–Gel Silica Modified with Covalently Bound Peptides. *J Phys Chem B* 2007;111:11850–7. <https://doi.org/10.1021/jp0744230>.

[80] Zheng X, Ke X, Yu P, Wang D, Pan S, Yang J, et al. A facile strategy to construct silk fibroin based GTR membranes with appropriate mechanical performance and enhanced osteogenic capacity. *J Mater Chem B* 2020;8:10407–15. <https://doi.org/10.1039/D0TB01962C>.

[81] Pantea D, Darmstadt H, Kaliaguine S, Roy C. Electrical conductivity of conductive carbon blacks: influence of surface chemistry and topology. *Applied Surface Science* 2003;217:181–93. [https://doi.org/10.1016/S0169-4332\(03\)00550-6](https://doi.org/10.1016/S0169-4332(03)00550-6).

[82] Hsu LC, Fang J, Borca-Tasciuc DA, Worobo RW, Moraru CI. Effect of micro- and nanoscale topography on the adhesion of bacterial cells to solid surfaces. *Applied and Environmental Microbiology* 2013;79:2703–12. <https://doi.org/10.1128/AEM.03436-12>.

[83] Cordero M, Mitarai N, Jauffred L. Motility mediates satellite formation in confined biofilms. *ISME J* 2023;17:1819–27. <https://doi.org/10.1038/s41396-023-01494-x>.

[84] Gülez G, Dechesne A, Smets B. The Pressurized Porous Surface Model: An improved tool to study bacterial behavior under a wide range of environmentally relevant matrik potentials. *Journal of Microbiological Methods* 2010;82:324–6. <https://doi.org/10.1016/j.mimet.2010.06.009>.

[85] Friedlander RS, Vlamakis H, Kim P, Khan M, Kolter R, Aizenberg J. Bacterial flagella explore microscale hummocks and hollows to increase adhesion. *Proceedings of the National Academy of Sciences* 2013;110:5624–9. <https://doi.org/10.1073/pnas.1219662110>.

[86] Jin X, Marshall JS. Mechanics of biofilms formed of bacteria with fimbriae appendages. *PLOS ONE* 2020;15:e0243280. <https://doi.org/10.1371/journal.pone.0243280>.

[87] Bjarnsholt T. Introduction to Biofilms. In: Bjarnsholt T, Jensen PØ, Moser C, Høiby N, editors. *Biofilm Infections*, New York, NY: Springer; 2011, p. 1–9. https://doi.org/10.1007/978-1-4419-6084-9_1.

[88] Seo H, Yu X, Tripathi A, Champion JA, Harris TAL. Enhancing Bacterial Adhesion with Hydro-Softened Chitosan Films. *ACS Macro Lett* 2025;14:1155–61. <https://doi.org/10.1021/acsmacrolett.5c00374>.

[89] Srinivasan R, Santhakumari S, Poonguzhali P, Geetha M, Dyavaiah M, Xiangmin L. Bacterial Biofilm Inhibition: A Focused Review on Recent Therapeutic Strategies for Combating the Biofilm Mediated Infections. *Front Microbiol* 2021;12. <https://doi.org/10.3389/fmicb.2021.676458>.

[90] Cardinali MA, Pierantoni DC, Comez L, Conti A, Chiesa I, Maria CD, et al. Black phosphorus/silk fibroin films hamper filamentous and invasive growth of *Candida albicans*. *RSC Adv* 2024;14:39112–21. <https://doi.org/10.1039/D4RA05126B>.

[91] Horsthemke M, Bachg AC, Groll K, Mozzio S, Müther B, Hemkemeyer SA, et al. Multiple roles of filopodial dynamics in particle capture and phagocytosis and phenotypes of Cdc42 and Myo10 deletion. *J Biol Chem* 2017;292:7258–73. <https://doi.org/10.1074/jbc.M116.766923>.

[92] Möller J, Lühmann T, Chabria M, Hall H, Vogel V. Macrophages lift off surface-bound bacteria using a filopodium-lamellipodium hook-and-shovel mechanism. *Sci Rep* 2013;3:2884. <https://doi.org/10.1038/srep02884>.

[93] Lam J, Herant M, Dembo M, Heinrich V. Baseline Mechanical Characterization of J774 Macrophages. *Biophysical Journal* 2009;96:248–54. <https://doi.org/10.1529/biophysj.108.139154>.

[94] Kocourková K, Kadlecová M, Wrzecionko E, Mikulka F, Knechtová E, Černá P, et al. Silk Fibroin Surface Engineering Using Phase Separation Approaches for Enhanced Cell Adhesion and Proliferation. *ACS Appl Mater Interfaces* 2025;17:13702–12. <https://doi.org/10.1021/acsami.5c00874>.

[95] Francius G, Polyakov P, Merlin J, Abe Y, Ghigo J-M, Merlin C, et al. Bacterial Surface Appendages Strongly Impact Nanomechanical and Electrokinetic Properties of *Escherichia coli* Cells Subjected to Osmotic Stress. *PLOS ONE* 2011;6:e20066. <https://doi.org/10.1371/journal.pone.0020066>.

[96] Alkhalifa S, Jennings MC, Granata D, Klein M, Wuest WM, Minbile KPC, et al. Analysis of the Destabilization of Bacterial Membranes by Quaternary Ammonium Compounds: A Combined Experimental and Computational Study. *ChemBioChem* 2020;21:1510–6. <https://doi.org/10.1002/cbic.201900698>.

[97] Jiang W, Saxena A, Song B, Ward BB, Beveridge TJ, Myneni SCB. Elucidation of Functional Groups on Gram-Positive and Gram-Negative Bacterial Surfaces Using Infrared Spectroscopy. *Langmuir* 2004;20:11433–42. <https://doi.org/10.1021/la049043+>.

[98] Oh JK, Yegin Y, Yang F, Zhang M, Li J, Huang S, et al. The influence of surface chemistry on the kinetics and thermodynamics of bacterial adhesion. *Sci Rep* 2018;8:17247. <https://doi.org/10.1038/s41598-018-35343-1>.

[99] Kovari DT, Wei W, Chang P, Toro J-S, Beach RF, Chambers D, et al. Frustrated Phagocytic Spreading of J774A-1 Macrophages Ends in Myosin II-Dependent Contraction. *Biophys J* 2016;111:2698–710. <https://doi.org/10.1016/j.bpj.2016.11.009>.

[100] Walkey CD, Olsen JB, Guo H, Emili A, Chan WCW. Nanoparticle Size and Surface Chemistry Determine Serum Protein Adsorption and Macrophage Uptake. *J Am Chem Soc* 2012;134:2139–47. <https://doi.org/10.1021/ja2084338>.

[101] Wold S, Sjöström M, Eriksson L. PLS-regression: a basic tool of chemometrics. *Chemometrics and Intelligent Laboratory Systems* 2001;58:109–30. [https://doi.org/10.1016/S0169-7439\(01\)00155-1](https://doi.org/10.1016/S0169-7439(01)00155-1).

[102] Wold S, Kettaneh N, Tjøssem K. Hierarchical multiblock PLS and PC models for easier model interpretation and as an alternative to variable selection. *Journal of Chemometrics* 1996;10:463–82. [https://doi.org/10.1002/\(SICI\)1099-128X\(199609\)10:5/6%253C463::AID-CEM445%253E3.0.CO;2-L](https://doi.org/10.1002/(SICI)1099-128X(199609)10:5/6%253C463::AID-CEM445%253E3.0.CO;2-L).

[103] Kuligowski J, Pérez-Rubio Á, Moreno-Torres M, Soluyanova P, Pérez-Rojas J, Rienda I, et al. Cluster-Partial Least Squares (c-PLS) regression analysis: Application to miRNA and

metabolomic data. *Analytica Chimica Acta* 2024;1286:342052.
<https://doi.org/10.1016/j.aca.2023.342052>.